

Lattice matched heterogeneous nucleation eliminate defective buried interface in halide perovskites

Paramvir Ahlawat^{1*}, Cecilia Clementi^{2,3,4}, Félix Musil²,
Maria-Andreea Filip¹

¹Yusuf Hamied Department of Chemistry, University of Cambridge,
Lensfield Road, Cambridge, CB2 1EW, United Kingdom.

²Department of Physics, Freie Universität Berlin, Arnimallee 12, 14195
Berlin, Germany.

³Department of Chemistry, Rice University, Houston, Texas 77005,
United States.

⁴Center for Theoretical Biological Physics, Rice University, Houston,
Texas 77005, United States.

Abstract

Metal halide perovskite-based semi-conducting hetero-structures have emerged as promising electronics for solar cells, light-emitting diodes, detectors, and photo-catalysts. Perovskites' efficiency, electronic properties and their long-term stability directly depend on their morphology [1–24]. Therefore, to manufacture stable and higher efficiency perovskite solar cells and electronics, it is now crucial to understand their micro-structure evolution. In this study, we perform molecular dynamics simulations to investigate the formation of cesium lead bromide perovskite on interfaces. Our simulations reveal that perovskite crystallizes in a heteroepitaxial manner on widely employed oxide interfaces. This could introduce the formation of dislocations, voids and defects in the buried interface, and grain boundaries in the bulk crystal. From simulations, we find that lattice-matched interfaces could enable epitaxial ordered growth of perovskites and may prevent defect formation in the buried interface.

*Correspondence to paramvir.chem@gmail.com

1 Introduction

Cesium lead bromide [25] has emerged as a versatile all-inorganic perovskite with applications spanning light-emitting diodes [26–29], liquid crystal displays [30, 31], photo-detectors [32], photo-catalysts [33–35], and perovskite solar cells (PSCs) [36–38]. Remarkably, this material exhibits room-temperature macroscopic quantum phenomena, such as super-fluorescence [39–44], arising from a quantum-coherent ensemble similar to the Bose-Einstein condensate. This material is actively utilized in the fabrication of certified all-perovskite tandem solar cells achieving solar-to-power conversion efficiencies exceeding 28% [45–47] surpassing the market-leading silicon-based solar cells. Furthermore, in perovskite-silicon tandem configurations, this material has been employed as a thermodynamically stable perovskite among mixtures to develop certified solar cells with efficiencies exceeding 30% [47–49], surpassing the efficiency of gallium arsenide-based solar cells. In the past decade, several experiments [15, 19, 50–54] have been conducted to improve the control over the shape, size, composition, and quality of the synthesized cesium lead bromide (CsPbBr_3) perovskite crystals. These experiments involved diverse methodologies, including solution processing, melt crystallization, and vapor deposition. Protesescu *et al.* [55] pioneered a shape-controlled synthesis approach using a hot-injection methodology, manipulating reaction temperatures. Subsequently, ligand-mediated synthesis protocols [56, 57] were introduced, incorporating organic molecules during growth. Pan *et al.* [58] and Sichert *et al.* [59] employed variable chain length carboxylic acids and amines to control nanocube and nanoplatelet dimensions. Liu *et al.* [60] and Wu *et al.* [61] further improved synthesis by introducing branched capping trioctylphosphine molecules, enhancing electronic properties.

However, solvent and organic molecular additives, while beneficial for shaping, can introduce defects, affecting stability and optoelectronic properties [62–64]. Alternatively, CsPbBr_3 can be manufactured through melt processing or vapor deposition, offering advantages like the synthesis of large single crystals [65–68]. Currently, there are many ongoing efforts at both the academic [19, 21, 22, 53, 69–77] and the industrial (Quantum Solutions [78], Avantama [31], Peroled [79], Nanolumi [80], Zhijing Nanotech [81] and Helio Display Materials [30]) level to improve existing synthesis processes and create new ones by using various additives and optimizing process conditions for enhancing the crystalline microstructure of halide perovskites.

To achieve precise control over CsPbBr_3 crystalline morphology, one requires an understanding of its nucleation and growth processes at the atomic scale. Ongoing experimental efforts often heavily rely on trial-and-error engineering approaches, while few groups endeavor to characterize the morphology of the synthesized crystals. In recent studies, Manna and collaborators [82] utilized X-ray crystallography, while Kovalenko and co-workers [83] employed *in-situ* optical absorption spectroscopy to examine the size and shape evolution of locally nucleated structures. However, the spatial and temporal resolution of state-of-the-art experimental techniques is often too limited to resolve nucleation processes accurately. Recently, advancements in *in-situ* transmission electron microscopy (TEM) [84, 85] have allowed for atomic-level

visualization of phase transitions. Nevertheless, the electron-beam sensitivity of halide perovskites, coupled with their soft nature, presents challenges in comprehending their crystallization mechanism through TEM experiments. Despite its fundamental importance and critical role in defining device stability and efficiencies, the crystallization mechanism of halide perovskites remains elusive, underlying the need for a more comprehensive understanding of these materials.

Alternatively, all-atom molecular dynamics (MD) simulations [86–105] offer a powerful methodology for describing atomic-level details of nucleation and growth processes [106–110], facilitating the design of more targeted and improved experiments [108]. In this study, we conduct all-atom MD simulations to explore perovskite nucleation from a homogeneous mixture of ions on interfaces.

2 Results

First, we perform simplified *ab-initio* quantum chemical calculations to develop a scaled-charge [111, 112] inter-atomic potential specifically tailored for perovskite, further details are provided in the Methods section. This potential predicts a melting temperature (T_m) of around 1000K, as determined by co-existing simulations depicted in Figure 1, see Methods section for details. Our predicted T_m value falls within a 20% range of the experimentally determined melting temperature (T_{expm}) of 860 ± 40 K [32, 113, 114]. Given the absence of experimental data on the dynamical aspects of perovskite crystallization at the nanosecond timescales, we also conducted a comparative analysis of the crystallization process. This involved comparing the performance of our scaled-charge inter-atomic potential with that of a more expressive machine learning interatomic potential (MLIP) generated by the NEQUIP [115] code using r2SCAN+rVV10 level density functional theory (DFT) reference data, as outlined in the Methods section. In Figure 1, our results demonstrate that in both scenarios, perovskite growth and melting events occur at the nanosecond timescale, underscoring the efficacy of our computational models in capturing these dynamic processes.

Homogeneous nucleation

We then start to study the process of homogeneous nucleation in perovskite, a critical step in its morphological evolution, using MD simulations with the scaled charge inter-atomic potentials. We initiated our simulations by constructing a system comprising 2560 ions, equivalent to the 512 formula units of CsPbBr_3 , within a periodic cubic box under atmospheric pressure. Under constant temperature-pressure MD simulations, we systematically cooled the systems to temperatures 10%, 20%, 25%, 30%, and 40% below the perovskite calculated melting temperature (T_m). Interestingly, at cooling levels of 30% and 40%, we observe the spontaneous emergence of the perovskite structure. Upon further inspecting the atomic level details of the crystallization process, we observe a non-spherical nucleus, already exhibiting macroscopic morphological features characteristic of a faceted crystal structure, as illustrated in Figure 2B

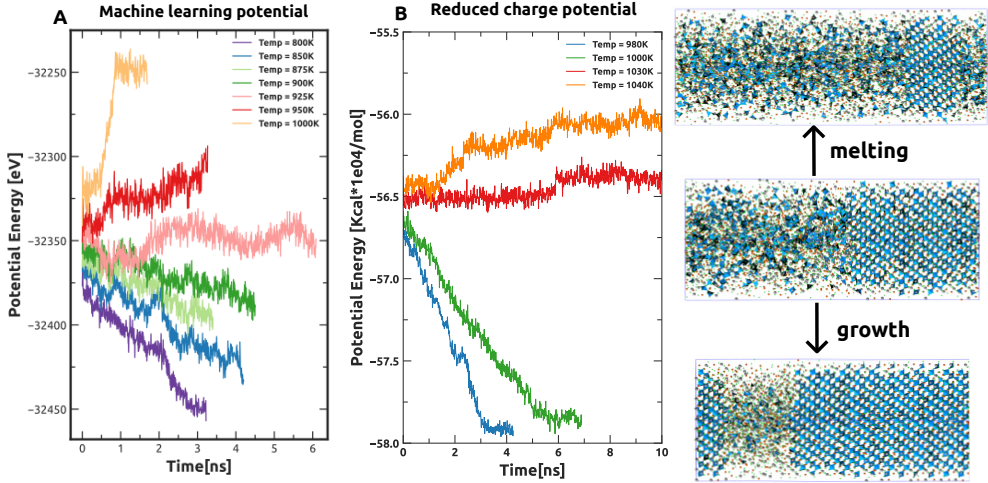


Fig. 1 Co-existing simulations: The figure illustrates the changes in potential energy during crystal growth simulations at different temperatures. The panel on the right displays the co-existing configurations and their evolution during melting and growth processes.

and Supplementary Movie SM1. This behavior is similar to the observations of previously studied ionic systems such as NaCl [91]. It is crucial to note that nucleation is a stochastic process, and our simulations, replicated with different momenta under constant 26% cooling conditions, exhibit a consistent behavior, as shown in Figure 2F. However, as the degree of cooling decreased below 20%, no discernible perovskite formation is observed in our extensive $\sim 1\mu$ second-long of brute force MD simulations. This suggests that nucleation events may become rare events at lower cooling rates, and we may require extensive sampling to understand the dynamics governing perovskite crystallization.

In our investigation of the crystallization process, we also aim to unravel the intricate structural transitions within multi-species systems such as the one in this study. We introduce a novel collective variable (CV), denoted by $K(L, X)$, that combines a general representation of the atomic neighborhood with the use of target configurations. The **landmark-SOAP CV** is based on the SOAP kernel [117, 118] where we compare the structural similarity[119, 120] between handpicked landmark configurations L , e.g. perfect perovskite crystals, and a set of configurations X , see the Methods section for more details. The SOAP representation of a local neighborhood is general [121], so it is tailored to distinguishing between the liquid and perovskite phases of CsPbBr₃ by comparing new configurations with perfect perovskite configurations. Figure 2D shows the probability distributions [122, 123] of $K(L, X)$, derived from a combination of molecular dynamics trajectories representing both the perovskite crystal and its molten structure. In particular, a $K(L, X)$ value exceeding 0.85 signifies ions associated with the perovskite structure, thereby facilitating the quantification of the perovskite fraction during the nucleation process. While our current study does not include calculations of nucleation rates, it is important to highlight the potential

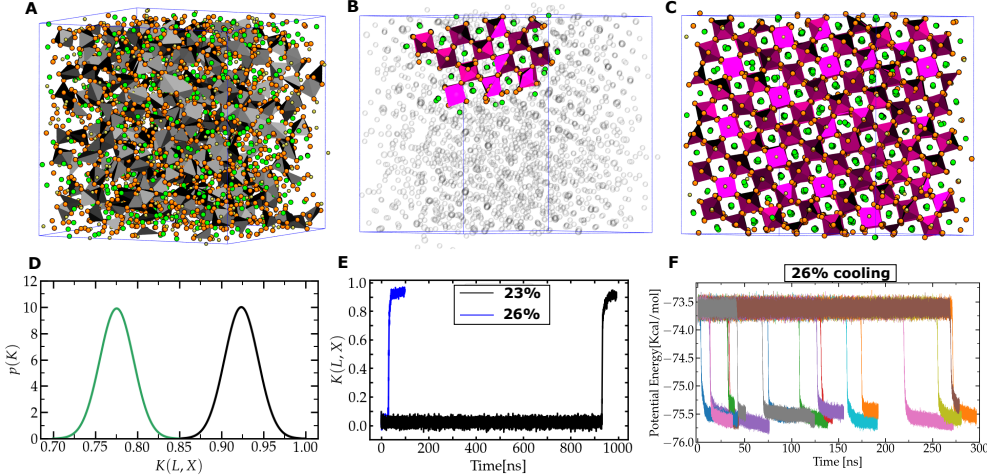


Fig. 2 Homogeneous nucleation of a perovskite: (a) shows the initial homogeneous mixtures of ions. Pb-Br complexes are shown as polyhedra with Pb in the center and Br in the corners. Free Cs and Br are shown as green and orange spheres respectively. (a)-(c) shows the evolution of homogeneous nucleation of perovskites at $\sim 26\%$ cooling with (a) being the initial homogeneous mixtures of ions. To guide the eye we show Pb-Br octahedra with separate colors for homogeneous mixtures (a) and crystalline perovskite structures in (b) and (c). (d) shows the probability distribution of SOAP similarity index ($K(\mathbf{L}, \mathbf{X})$) for homogeneous melt (green) and perovskite phase (black) of CsPbBr_3 . (e) shows the time evolution of normalized $K(\mathbf{L}, \mathbf{X})$ values for the MD trajectory at two different supercooled temperatures. (f) represents the time evolution of the potential energy at $\sim 26\%$ supercooling with variable momenta. All of the above nucleation images are generated with VMD [116].

of $K(L, X)$ in extending our understanding to include such analyses. Specifically, by analyzing mean free passage time data obtained from repeated simulations at various cooling rates, $K(L, X)$ can be extended to calculate nucleation rates in these multi-species systems. Such insights hold promise for elucidating the kinetics underlying complex structural transformations in a diverse range of multi-component materials.

For our system, the temporal evolution of $K(L, X)$ presented in Figure 2E unveils a distinctive first-order phase transition during the nucleation of perovskite, devoid of any intermediate meta-stable phases. However, subsequent investigations of post-nucleation crystals reveal the emergence of bulk quasi-two-dimensional Ruddleson-Popper (RP) faults. These planar boundary anti-phase structures are characterized by two consecutive $[\text{CsBr}]$ layers between neighboring $[\text{Pb}-\text{Br}]$ octahedral sites within the perovskite, also highlighted in Figures 3A and Supplementary Figure 1. We extracted the RP-faulted structures from our nucleated trajectories and conducted variable-cell-relaxation using DFT. Notably, the structures persist in their RP form, and the DFT-optimized configurations are included in the Supplementary Material. Significantly, the presence of RP-faults in CsPbBr_3 is corroborated by experimental findings [124], with various atomic-level TEM measurements detecting these structural features in bulk perovskite thin-films. To further investigate the process of RP

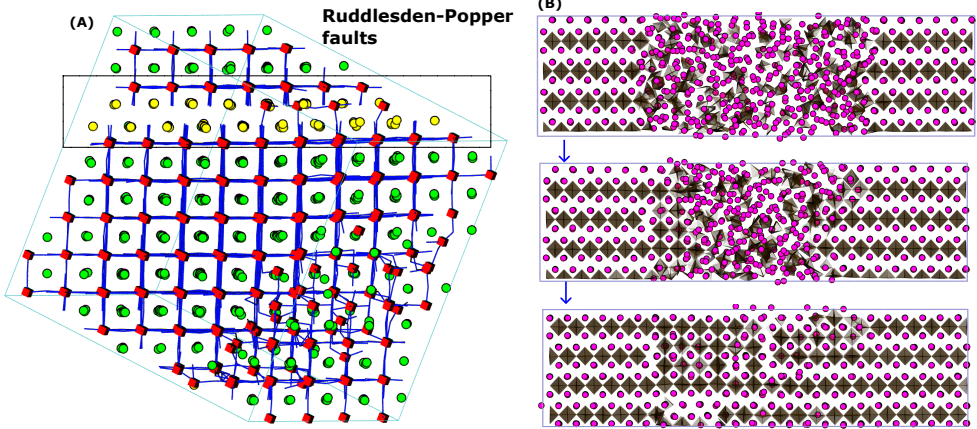


Fig. 3 Ruddlesden-Popper (RP) faults: (A) shows RP-faults in a nucleated crystal. (B) illustrates the co-existing simulations of the RP structure alongside a homogeneous mixture of ions.

structures' formation, we carried out co-existing simulations of quasi-2D Cs_2PbBr_4 seeded structure alongside a homogeneous mixture of ions, as illustrated in Figure 3B and Supplementary Movie SM2. Surprisingly, even in the presence of quasi-2D seeds, we observe the crystallization of mixed quasi-2D and 3D perovskite configurations. Therefore, it is unlikely that these anti-phase RP faults form in bulk during the nucleation of CsPbBr_3 perovskite, suggesting their possible formation at boundaries when two growth fronts interact with each other.

Experimental investigations [125] have revealed that the density of RP faults in CsPbBr_3 can significantly impact its photoluminescence properties. Moreover, RP-faulted structures are not exclusive to CsPbBr_3 , and they have been observed in various materials. For example, recent TEM experiments [126, 127] have linked pre-melting phenomena in oxide perovskites to the presence of RP faults. Notably, a study demonstrated a substantial increase in the superconducting temperature of nickelates [128] upon the elimination of these RP-faulted structures by optimizing their heterogeneous crystallization process. Our simulation findings are in line with experimental measurements across a diverse range of perovskite systems, underscoring the complexity of the crystallization process in multi-species systems, where various condensed phases can emerge. The L-SOAP-CV plays an important role in enabling the differentiation between distinct phases and facilitating a comprehensive atomic-level understanding of the process. Motivated by these exciting observations and successful comparisons with experiments and calculations, we proceed to simulate nucleation on interfaces.

Crystallization on interfaces

We initiate the process by depositing a homogeneous mixture of ions onto a substrate. We construct simplified systems where Cs, Pb, and Br ions are arranged on the surface

of a commonly used anatase-TiO₂ substrate. For this study, we consider two different experimental setups: (A) the crystallization of perovskite on a single flat surface, and (B) the crystallization of perovskite sandwiched between flat surfaces. The latter condition mimics experimental conditions resembling the mesoporous architecture of the substrate, where perovskite may crystallize between large oxide nanoparticles.

Using these two setups, we conduct molecular dynamics (MD) simulations, as outlined in the Methods section. These simulations are performed at a cooling rate of 25% to prevent rapid perovskite crystallization. Through brute force MD simulations with setup (A), we observe the transformation of the initial ion mixture into the corner-sharing perovskite structure. Nucleation of perovskite initiates from the substrate, and subsequently, the ion mixture fully converts into a large perovskite crystal with accelerated growth. Given the stochastic nature of crystallization, we repeat our simulations five times, consistently observing substrate-induced heterogeneous nucleation of perovskite in all runs. No instances of homogeneous nucleation are observed in the repeated simulations. The complete crystallization process is illustrated in Figures 4D to H, with an atomic-level view provided in Supplementary Movie SM3.

Crystallization of semiconductors on interfaces typically manifests through three distinct modes: Frank–van der Merwe, Volmer–Weber, and Stranski–Krastanow. Key differences between these modes lie in how the initial crystalline layer nucleates on the interface, as depicted in Figures 4A, 4B, and 4C, respectively. Using the L-SOAP-CV, we characterize our simulations and investigate which of these mechanisms best describes the crystallization of perovskite on oxide substrates. We partition our simulation box into layers parallel to the substrate, with each layer represented by different colors in Figure 4D. The time evolution of perovskite octahedra in each layer is shown in Figure 4I.

The perovskite growth extends to the fourth (yellow) layer even before the complete crystallization of the first (blue) layer closest to the substrate. This observation is further illustrated in Figure 4E, where an island of perovskite has emerged within the simulation box. We note that despite appearing as separate entities, the two islands in Figure 4E are integral parts of the same crystal, owing to the periodic nature of our simulation box. This means that our analysis identifies the Volmer–Weber (VW) mechanism (illustrated in Figure 4B) as governing the perovskite crystallization. This mechanism is also reminiscent of highly mismatched growth in heterostructures as it entails island-type growth on the substrate without the formation of a wetting layer. The significant lattice mismatch between the unit cells of anatase-(101) ($a=b=3.776\text{\AA}$, $c=9.486\text{\AA}$) and perovskite ($a=b=c=5.87\text{\AA}$) emphasize the differences in their structures, and we do not observe significant density fluctuations of ions near the interface before crystallization. The impact of VW crystallization on the morphological evolution of perovskite is shown in Figure 4G, where the convergence of two growth fronts leads to the formation of a highly defected buried interface and a grain boundary. Through subsequent analysis of the buried region and grain boundary, we observe that these regions exhibit dangling bonds and incomplete formation of Pb-Br octahedra. Interestingly, Pb-Br edge-sharing octahedra stacking faults [129] and dislocations

have crystallized in these regions, providing insights into the structural evolution of perovskite's buried interface.

Following setup (B), where a homogeneous mixture of ions is confined between flat TiO_2 interfaces, we conducted isothermal-isobaric simulations with moderate coolings for this system. Figure 5 provides a comprehensive view of the crystallization process, ranging from 5A, depicting the initial configuration, to 5F, representing the final crystallized state. Visual examination and atomic-level view provided in Supplementary Movie SM4 of these configurations, confirms the evident crystallization of perovskite on the substrate, as observed in Figure 5B. Once nucleated, the growth proceeds rapidly, with the growth front reaching the other interface before nucleation occurs on the opposite side. Similar to the previous case, we observe a VW mechanism of growth, leading to the formation of perovskite islands, as depicted in Figure 5C. Consistent with the previous system, we also observe the formation of grain boundaries and defective buried interfaces. However, a novel observation emerges in this case when the growth front reaches the other side. Notably, the formation of a nano-void is highlighted in Figure 5F. Upon investigation, we again find that the presence of non-stoichiometric edge-sharing octahedra at the grain boundary and buried interface leads to a depletion of ions available for forming complete corner-sharing octahedra. Consequently, the formation of nano-voids is attributed to the emergence of non-stoichiometric structures resulting from ion consumption in the VW crystallization.

In both scenarios, the evolution of the perovskite microstructure reveals heteroepitaxial crystallization, accompanied by the emergence of grain boundaries, stacking faults, dislocations, and nano-voids. Earlier spectroscopic experimental investigations [14, 130–133] have substantiated that grain boundaries, dislocations, and stacking faults are among the most detrimental defects and substantial contributors to the degradation of halide perovskites. Recent experiments have further highlighted the rapid degradation of PSCs in the presence of nano-voids in the buried interface. Therefore, the elimination of these defects is crucial for achieving a stable perovskite morphology and advancing the industrialization of PSCs. From the above mentioned results, now a fundamental question arises: how can the observed defects be eliminated?

Lattice Matched Interface

In pursuit of this objective, we draw inspiration from previous research work on the crystallization and development of semiconductor heterostructures [134, 135] and blue LEDs [136–138] and conduct MD simulations to study the lattice-matched perovskite crystallization. We construct an artificial lattice-matched substrate made of particles interacting by simplified Lennard-Jones (LJ) potential. An initial system is prepared by placing a homogeneous mixture of ions on this artificial perovskite-type LJ lattice (see Figure 6A). Subsequently, brute-force MD simulations are carried out at moderate coolings, and the time evolution of the crystallization process is shown in Figures 6A to 6D. The nucleation begins by forming a uniform layer of perovskite at the blue-colored interface, as shown in Figures 6B and in Supplementary Movie SM5. Unlike in

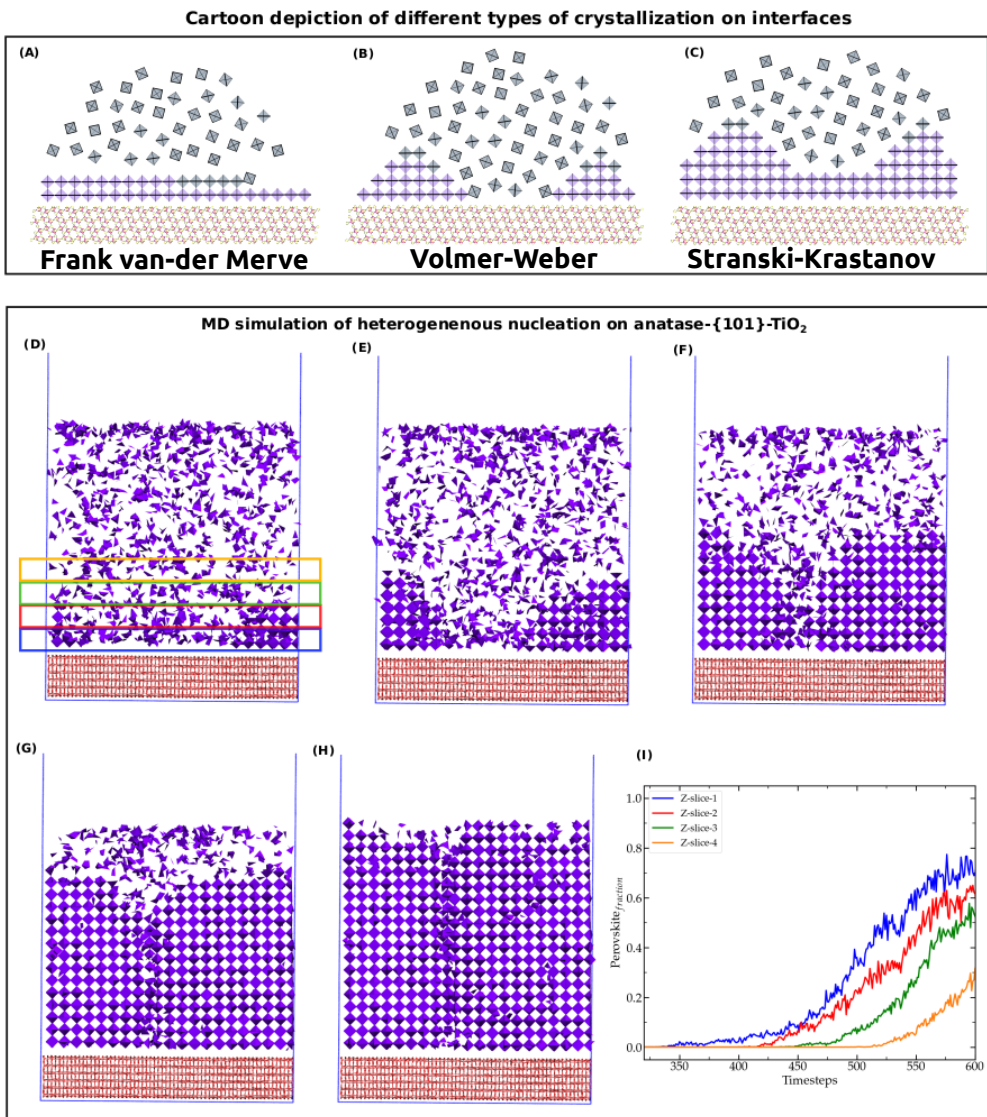


Fig. 4 Heterogeneous nucleation of a perovskite: (A), (B), and (C) present cartoon depictions of commonly identified crystallization mechanisms. Panels (D) to (H) provide a visual representation of the typical evolution of heterogeneous nucleation on the interface, with only violet-colored Pb-Br octahedra shown for clarity. Figure (I) illustrates the temporal changes in the amount of perovskite in different layers calculated using L-SOAP-CV, as highlighted by the boxed region in Figure (D). All images were generated using VMD [116].

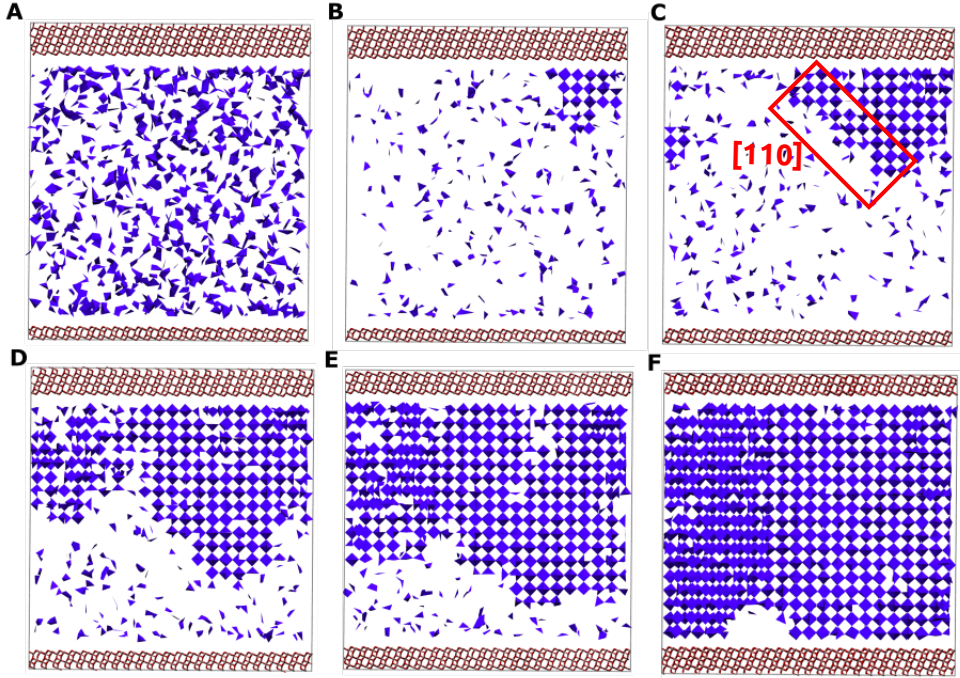


Fig. 5 Heterogeneous nucleation of a perovskite: Figures A to F illustrate the typical progression of perovskite crystallization between flat TiO_2 substrates. For clarity, only $\text{Pb}-\text{Br}$ octahedra are depicted in blue to facilitate the tracking and visualization of the crystallization process. The TiO_2 substrate is represented by a red-colored $\text{Ti}-\text{O}$ bonded network. Images are generated with VMD software [116].

the previous systems which followed the VW mechanism, the lattice-matched interface allows for the crystallization process to resemble the Stranski-Krastanov (SK) growth model (see Figure 4C) where a uniform layer crystallizes on the substrate first, followed by the growth of islands on that layer, as partially evident in Figure 6B.

Previous experiments [139] with different heterostructures have indicated that the Stranski-Krastanov (SK) type crystallization often involves density fluctuations at the interface, which help in forming a uniform crystalline layer. To explore this further, we examine the density of ions before and after crystallization, as depicted in Figure 7A. We observe a higher concentration of ions near the substrate, particularly Cs ions closest to it. This trend becomes more pronounced after perovskite crystallization, as shown in Figure 7C, where a complete layer of Cs ions forms on the substrate. This suggests that Cs ions may play a crucial role in promoting the uniform nucleation of the perovskite structure. To delve deeper into this phenomenon, we conduct additional simulations where we enhance the interaction strength between the substrate and the ions. Figure 7B shows that the number of Cs ions near the interface increases with stronger interaction. This effect is further emphasized in Figure 6F, where we observe

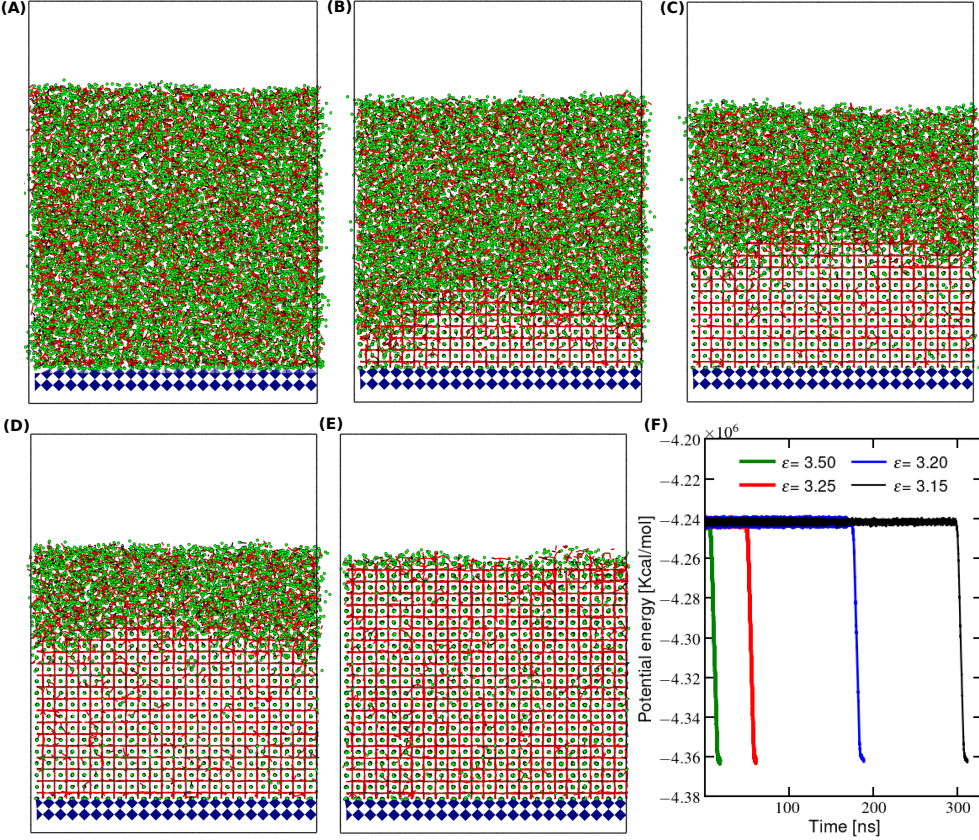


Fig. 6 Lattice matched interface: (A) to (E) show the evolution of crystallization on an artificial lattice-matched interface; (F) displays the time evolution of the potential energy with varying ion-substrate interaction strength.

an early decrease in potential energy, indicating the initiation of perovskite crystallization. To further validate these findings, we repeated the simulations multiple times and consistently observed similar outcomes. These results suggest that manipulating the interaction strength between the substrate and ions could potentially influence the nucleation and growth behavior of perovskite crystals, offering insights for controlling the crystallization process in future applications.

Finally, we investigate the differences in the bulk morphologies of perovskite crystals during lattice mismatch and lattice-matched crystallization processes. As highlighted in Figure 6(C), the Volmer-Webber dominated crystallization process predominantly exhibits [110]-faceted perovskite crystals. In simulations involving lattice-matched substrates, we examine the localized facet evolution by employing local structure factors within a defined cutoff of crystallized atoms. We monitor the time evolution of the averaged intensities of X-ray peaks assigned to corresponding [100],

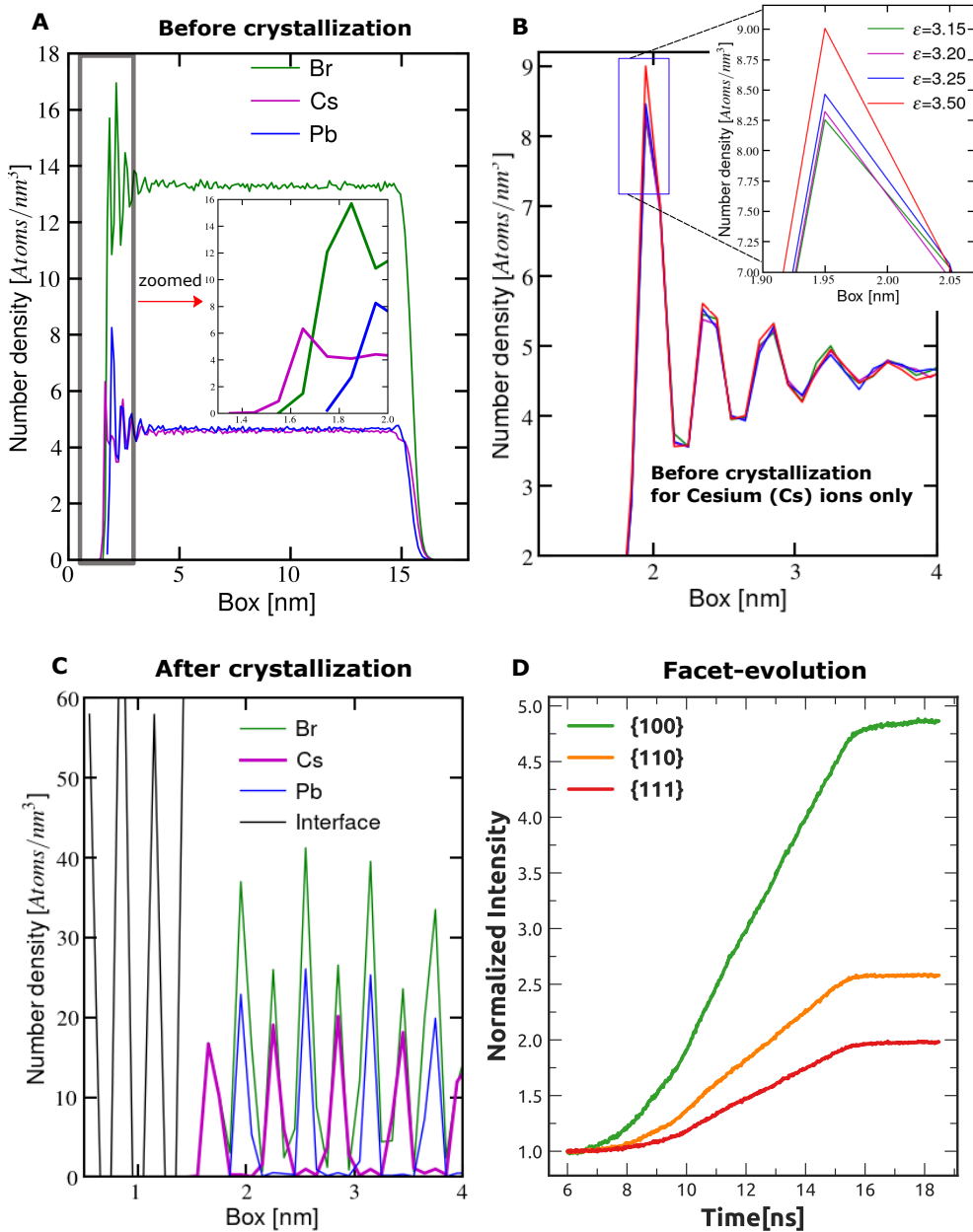


Fig. 7 Lattice matched interface: (A), (B) and (C) represent the density profiles, while (D) illustrates the time evolution of corresponding X-ray peaks using the local Debye structure factor during crystallization.

[110], and [111] facets in the perovskite structure. While our periodic simulations are too limited in size to predict macroscopic crystal shapes accurately, the analysis of local structure evolution offers valuable insights into facet preferences for atom adsorption, providing glimpses into the final crystal morphology. In particular, Figure 6(D) highlights that the crystal growth in lattice matching simulations is predominantly driven towards the [100]-faceted perovskite crystals direction.

3 Discussion and Conclusion

Understanding and controlling the crystallization of halide perovskites represents a significant challenge for their industrialization. In this study, we try to address this challenge by building from fundamental quantum chemistry calculations of ionic interactions, followed by elementary all-atom MD simulations of perovskites on interfaces. We successfully observe the direct homogeneous and heterogeneous nucleation of halide perovskites. Through our investigation, we uncovered the formation of buried dislocations, grain boundaries, and nano-voids. A key observation is that defect formation is favored in mismatched heteroepitaxial systems, while lattice-matched substrates exhibit a uniform layered growth mode.

A pivotal insight from our simulations also lies in the potential to induce perovskite crystallization by modulating the interaction of ions with the interface. Consequently, perovskites form on the substrate covered by a thin wetting layer. Introducing a buffer layer could be instrumental in reducing the interfacial free energy, thereby transforming heteroepitaxial crystallization into epitaxial growth and minimizing the density of defects in the buried interface. Recent experiments [140–143] have explored the use of various molecular additives to control the crystallization process and eliminate buried interfaces. However, the additives employed in halide perovskites are often selected through trial-and-error strategies. Further simulations and experiments would offer deeper insights into the impact of these additives on crystallization and help in the selection of specific types of molecular additives at interfaces. Moreover, recent experiments [22, 23] have also established that [100] facets exhibit superior electronic properties and stability compared to [110] and polar [111] surfaces.

While our primary study provides valuable insights, it is essential to acknowledge its inherent limitations. First, inter-atomic potential we developed for CsPbBr_3 heterostructure simulations is qualitative and lacks the inclusion of polarization effects and other perovskite polymorphs. Additionally, our simulations are performed with a simplified setup compared to experimental conditions, excluding the simulation of solution mixtures and the effects of various solvents and additives on heterogeneous nucleation. Furthermore, we did not account for the effects of different types and facets of oxide substrates along with the presence of molecular additives. In future research, we aim to address these limitations by developing more accurate MLIPs for perovskites and commonly employed substrates, accounting for polarization effects and simulating various large-scale heterostructures, including those involving solutions. We also plan to investigate the impact of commonly used oxide substrates, such as SnO_2 , NiO ,

and Al_2O_3 , on the buried interface. Additionally, we aim to explore oxide perovskite substrates, such as BaTiO_3 , which may demonstrate favorable lattice matching with halide perovskites.

With new developments in quantum chemical methodologies [144–151] and large scale MLIPs [152–155], our computational framework presented in this study offers promising opportunities for investigating complex structural transformations across a diverse range of multi-species perovskite materials, for example, perovskite superconductors [156–159], multiferroics [160], Josephson-junctions [161], essential battery components [162–165], fuel cells [166], and spintronics [167]. Achieving precise morphological control over heterostructures is crucial for advancing these materials toward industrial-scale applications.

4 Methods

4.1 Inter-atomic potential

We take inspiration from earlier studies [111, 112] on ionic species and construct a reduced point charge inter-atomic potential for CsPbBr_3 . To fit the remaining Pb parameters with the existing species of Cs and Br, we employ the Complete Active Space Self Consistent Field (CASSCF) method [168–170] to obtain binding curves for dimer fragments of the CsPbBr lattice, see Supplementary Figure 2. In this approach, one starts from a Hartree-Fock (HF) [171–174] reference determinant $|\Phi\rangle$, built from a set of parametrized molecular orbitals $\{\phi(\alpha)\}$, optimized to minimize the single-determinant energy,

$$\tilde{E} = \frac{\langle \Phi | \hat{H} | \Phi \rangle}{\langle \Phi | \Phi \rangle}, \quad (1)$$

where \hat{H} is the system Hamiltonian. Disjoint sets of core (always filled), virtual (always empty), and active orbitals are defined. The space of all Slater determinants obtained by rearranging the active electrons among the active orbitals while preserving the spin and point group symmetry of the original HF reference is known as a complete active space (CAS) and customary labeled as $(n_{\text{elec}}, n_{\text{orb}})$, where n_{elec} is the number of active electrons and n_{orb} is the number of active spatial orbitals. The CASSCF wavefunction form is given by a linear combination of all determinants belonging to the CAS,

$$|\Psi(\{\mathbf{c}_\mu\}, \{\alpha\})\rangle = \sum_{\mu \in \text{CAS}} c_\mu |\mu(\{\alpha\})\rangle, \quad (2)$$

where $|\mu\rangle$ denotes a Slater determinant. Both the parameters $\{\mathbf{c}_\mu\}$ and the underlying molecular orbital parameters $\{\alpha\}$ are then optimized simultaneously in a self-consistent procedure to minimize the resulting energy,

$$\tilde{E} = \frac{\langle \Psi | \hat{H} | \Psi \rangle}{\langle \Psi | \Psi \rangle}, \quad (3)$$

By allowing for orbital relaxation from the HF reference and the inclusion of multiple determinants of comparable weights, the CASSCF approach excels at capturing strong or static correlation effects and therefore provides good descriptions for dissociation binding curves. We run first-principle CASSCF calculations using an (8,8) CAS for closed-shell and a (7,8) CAS for open-shell species in the def2-TZVPP basis set [175–177], with corresponding effective core potentials, using the PySCF program [178] and extract the inter-atomic potential parameters listed in the Supplementary Information. Using these parameters, we find that the perovskite structure is stable in its original form at finite temperatures. We test this inter-atomic potential against finite temperature experimental lattice parameters and melting point by co-existing simulations illustrated in Supplementary Figure 2.

The CASSCF approach is very well-suited to study the strong correlation effects present in dissociation processes, but it scales exponentially with the size of the active space considered, making it challenging to expand to larger systems. Therefore, if we wish to expand this approach to more electrons or larger fragments, other methods may be necessary. Approaches based on Monte Carlo simulations of the wavefunction in Hilbert space have been shown to be effective in treating this type of problem, at reduced computational cost [144, 150, 151, 179, 180], while allowing for flexible definitions of the active space that may be optimized for the interaction in question.

4.2 Machine learning potential

The NequIP potentials [115, 181, 182] employed in this study are derived from *ab-initio* molecular dynamics (AIMD) simulations based on DFT. The training methodology involves the utilization of two interaction layers with a radial cutoff of 8Å, incorporating interatomic distances encoded within a basis comprising eight Bessel functions. Feature representations are selected up to rotation orders of L=2. The loss function incorporates forces, energies, and stresses obtained from DFT calculations. Optimization is performed using the Adam optimizer with a learning rate of 0.005 and a batch size of 10. The training process is executed on a V100 GPU.

4.3 DFT calculations

In this study, all DFT calculations are conducted employing the r²SCAN+rVV10 functional [183], with a 600 eV plane-wave-basis cutoff, PBE potentials, and the projector augmented wave (PAW) formalism for electronic minimization, implemented within the VASP (Vienna ab initio simulation package) code [184, 185]. To generate the training dataset, ab initio molecular dynamics (AIMD) simulations are carried out for 135-atom supercells, corresponding to a 3x3x3 unit cell of cubic-CsPbBr₃, including both crystalline and molten CsPbBr₃ phases at temperatures ranging from 600 K to 1000 K, with intervals of 100 K, for a duration of 2 ps. These simulations are performed under the isothermal-isobaric (NPT) ensemble, utilizing a time step of 2 fs. The pressure and temperature are maintained using the Parrinello-Rahman barostat [186] and the Langevin thermostat, respectively. For these relatively large supercells, only Gamma point sampling in the Brillouin zone is employed. The melted configuration is obtained by heating the crystal to a very high temperature of 2300 K.

4.4 Landmark-SOAP Collective Variable (L-SOAP-CV)

Crystallization in multi-species materials is a complex phenomenon characterized by the emergence of a crystalline nucleus through the local ordering of diverse chemical species. Various CVs, often tailored to specific systems or phases, have been introduced to quantify and scrutinize the intricacies of the crystallization process. Inspired by prior investigations on phase transitions, we draw insights from studies on bond-orientational order parameters [187], accurate particle-based measures [188], and morphology-aided order parameters [189–191]. Taking inspiration from these foundations, we formulate simplified one-dimensional CVs and hereafter, we provide details on the **landmark-SOAP** CV and its application in the present study. In essence, we propose applying the SOAP kernel [117] to measure the similarity between hand-picked landmark atomic environments, effectively defining the target local nucleated states, and atomic structures, e.g. extracted from nucleation simulations. The SOAP representation [117] characterizes the neighborhood of an atom i within an atomic structure X by extracting invariant n -body correlations from the atomic density field

$$\rho(\mathbf{r}, a; X_i, r_c, \sigma) = \sum_{j \in X_i} \delta_{aa_j} \exp\left[\frac{(\mathbf{r} - \mathbf{r}_{ij})^2}{2\sigma^2}\right] f_c(r_{ij}), \quad (4)$$

where the sum $\sum_{j \in X_i}$ runs over the atoms j of type a_j (including atom i) that belong the neighborhood of atom i , $\mathbf{r}_{ij} = \mathbf{r}_j - \mathbf{r}_i$, $r_{ij} = \|\mathbf{r}_{ij}\|$, f_c is a smooth cutoff function with cutoff radius r_c , and σ is a smoothing parameter. For simplicity, we focus on the SOAP powerspectrum expanded on a basis of radial functions and spherical harmonics given by

$$p_{a_1 n_1 a_2 n_2 l}^{(i)} = \frac{1}{\sqrt{2l+1}} \sum_m (-1)^m c_{a_1 n_1 lm}^{(i)} c_{a_2 n_2 l(-m)}^{(i)}, \quad (5)$$

where $c_{a n l m}^{(i)}$ are the expansion coefficients of the density field (see Ref. [192] for the full expression), and the indices n and (l,m) refer to the radial basis and spherical harmonics. The SOAP powerspectrum coefficients are invariant with respect to atom permutations, global translations, global rotations, and reflections of the atomic coordinates. Moreover, they encode the 3-body correlations within the environment of atom i with the different atomic identities present in the system. Therefore, this representation is able to differentiate with great accuracy a wide range of atomic environments. [118, 193] To transform the characterization of atomic neighborhoods given by the SOAP representations into a CV, we use the SOAP kernel [117]

$$k_\zeta(L_i, X_j) = \left[\frac{\mathbf{p}^{(L_i)} \cdot \mathbf{p}^{(X_j)}}{\|\mathbf{p}^{(L_i)}\| \|\mathbf{p}^{(X_j)}\|} \right]^\zeta, \quad (6)$$

to measure the similarity of the environment of atom L_i and atom X_j through the lens of the SOAP powerspectrum. Note that this similarity measure has the same properties [121] (invariances, information content, ...) as the representation it is based on, e.g. two configurations that are a reflection of each other look identical with this metric. To make this CV more concrete, we take the example of the nucleation of

perovskite. We measure the similarity between landmark environments $\{L_i\}_{i=1,\dots,R}$ extracted from the perfect perovskite crystal, e.g. centering on the Pb atoms, with comparable environments extracted from nucleation simulations, we can estimate the fraction of the material X that has nucleated

$$N_c(X) = \sum_j \sigma_{m,k} (\text{softmax}[k_\zeta(L_1, X_j), \dots, k_\zeta(L_R, X_j)]) \quad (7)$$

where $\sigma_{m,k}(x) = \frac{1}{2} \left(\tanh\left[\frac{k(2x' - 1)}{2\sqrt{x' - x^2}}\right] + 1 \right)$ with $x' = x - m + 0.5$ is a switching function, and the parameters m and k control respectively the position and the steepness of the switch. Typical values are $m = 0.97$ and $k = 200$. We note here that the versatility of the SOAP representation [117, 121] ensures that the landmark-SOAP CV can be applied to a wide range of materials while the use of landmark environments allows for tuning this CV to resolve the differences between many condensed polymorphs.

4.5 Details of MD simulations with LAMMPS

Before performing production runs, we achieve system equilibration through 10 ns isothermal-isobaric simulations conducted above the melting temperature. Our simulations employ a 1.0 nm cutoff for nonbonded interactions, particle-mesh Ewald for handling electrostatic interactions, a velocity re-scaling thermostat [194] with a relaxation time of 0.1 ps for temperature control, and a Parrinello-Rahman barostat [186] for pressure control, featuring a relaxation time of 10 ps. The classical molecular dynamics simulations are executed using the Large-Scale Atomic/Molecular Massively Parallel Simulator (LAMMPS) code (version 31 Mar 2017) [195].

4.5.1 Co-existing simulations

The initial structures as illustrated in Figure 1 are constructed by combining seeded structures of CsPbBr_3 with the molten configuration. Seeds oriented along [100], [110] and [111] directions are generated using ASE utilities. Melted configurations are created either by melting crystalline seeds at elevated temperatures via inter-atomic potentials or by generating supercells directly from molten structures through AIMD simulations. The final configuration involves an equal number of atoms in seed and melt: 768 f.u. for scaled charge based simulations and 128 f.u. for MLIPs. The MLIP-based simulations are conducted using the *pair_nequip* interface with LAMMPS code.

4.5.2 Crystallization on interfaces

The simulation systems shown in Figures 4 and 5 are prepared by depositing homogeneous mixtures of ions on flat (101)-anatase-TiO₂ substrate. A point charge inter-atomic potential [196, 197] was used for TiO₂. During constant volume simulations, substrates are kept frozen. For lattice-matched simulations in Figure 6, we prepared a larger simplified perovskite lattice with a similar lattice constant as CsPbBr_3 and particle-particle inter-actions are described by Lennard-Jones (LJ) potential. Lattice matched simulations consist of approximately 60000 atoms.

Supporting Materials.

- Perovskite-simulations.ipynb: A python-notebook to perform MD simulations of perovskites
- Quantum-chemistry.ipynb: A python-notebook to perform CASSCF calculations in PySCF
- SOAP-analysis.ipynb: A python-notebook to perform SOAP calculations
- All simulations data-set including trajectories: 10.5281/zenodo.10975237

Acknowledgements. This research is funded by Swiss National Science Foundation (SNSF) Postdoc.Mobility fellowship P500PN_206693. F.M. acknowledges support from the SNSF under the Postdoc.Mobility fellowship P500PT_203124, and from the Physics department and Freie Universität Berlin for computing time. M.A.F. is grateful to Peterhouse, University of Cambridge for support through a Research Fellowship. P.A. is indebted and greatly thankful to Yusuf Hamied Department of Chemistry for hosting and providing necessary computational resources through Rogue-GPU cluster, Nest-CPU cluster, UK Materials and Molecular Modelling Hub YOUNG CPU/GPU cluster, which is partially funded by EPSRC (EP/T022213/1, EP/W032260/1 and EP/P020194/1). This work used the ARCHER2 UK National Supercomputing Service (<https://www.archer2.ac.uk>). P.A. is immensely thankful to Professor Daan Frenkel for several key discussions, large dose of encouragements and key guidance that led to fruition of this research. P.A. is sincerely thankful to Professors Michael Graetzel, Angelos Michaelides, Mike Payne, Alex Thom, Ali Alavi, Carlos Vega, Peter Bolhuis, Rob Jack, Alessandro Laio, Rachel Oliver, Erin Johnson and Michiel Sprik for highly inspiring and insightful discussions.

Contributions. P.A. conceived, formulated and conceptualized research. M.A.F. designed and performed CASSCF calculations. F.M. created L-SOAP-CV and designed an interface with PLUMED2 software. P.A. designed both classical and machine learning interatomic potentials, designed and performed all classical, MLIPs and *ab-initio* MD simulations, and conducted analysis. C.C. read the manuscript and provided some comments. P.A., M.A.F and F.M. discussed research and wrote the manuscript together.

Declarations. Authors declare no conflicting interest.

References

- [1] Mitzi, D.B., Feild, C.A., Schlesinger, Z., Laibowitz, R.B.: Transport, Optical, and Magnetic Properties of the Conducting Halide Perovskite CH₃NH₃SnI₃. Journal of Solid State Chemistry **114**(1), 159–163 (1995) <https://doi.org/10.1006/jssc.1995.1023> . Accessed 2024-02-29
- [2] Mitzi, D.B., Wang, S., Feild, C.A., Chess, C.A., Guloy, A.M.: Conducting Layered Organic-inorganic Halides Containing ⟨110⟩-Oriented Perovskite Sheets. Science **267**(5203), 1473–1476 (1995) <https://doi.org/10.1126/science.267.5203.1473>

- [3] Kojima, A., Teshima, K., Shirai, Y., Miyasaka, T.: Organometal Halide Perovskites as Visible-Light Sensitizers for Photovoltaic Cells. *Journal of the American Chemical Society* **131**(17), 6050–6051 (2009) <https://doi.org/10.1021/ja809598r> . Accessed 2024-02-29
- [4] Lee, M.M., Teuscher, J., Miyasaka, T., Murakami, T.N., Snaith, H.J.: Efficient Hybrid Solar Cells Based on Meso-Superstructured Organometal Halide Perovskites. *Science* **338**(6107), 643–647 (2012) <https://doi.org/10.1126/science.1228604> . Accessed 2024-02-29
- [5] Kim, H.-S., Lee, C.-R., Im, J.-H., Lee, K.-B., Moehl, T., Marchioro, A., Moon, S.-J., Humphry-Baker, R., Yum, J.-H., Moser, J.E., Grätzel, M., Park, N.-G.: Lead Iodide Perovskite Sensitized All-Solid-State Submicron Thin Film Mesoscopic Solar Cell with Efficiency Exceeding 9%. *Scientific Reports* **2**(1), 591 (2012) <https://doi.org/10.1038/srep00591> . Accessed 2024-02-29
- [6] Burschka, J., Pellet, N., Moon, S.-J., Humphry-Baker, R., Gao, P., Nazeeruddin, M.K., Grätzel, M.: Sequential deposition as a route to high-performance perovskite-sensitized solar cells. *Nature* **499**(7458), 316–319 (2013) <https://doi.org/10.1038/nature12340> . Accessed 2024-02-29
- [7] Snaith, H.J., Abate, A., Ball, J.M., Eperon, G.E., Leijtens, T., Noel, N.K., Stranks, S.D., Wang, J.T.-W., Wojciechowski, K., Zhang, W.: Anomalous Hysteresis in Perovskite Solar Cells. *The Journal of Physical Chemistry Letters* **5**(9), 1511–1515 (2014) <https://doi.org/10.1021/jz500113x> . Accessed 2024-02-29
- [8] De Quilettes, D.W., Vorpahl, S.M., Stranks, S.D., Nagaoka, H., Eperon, G.E., Ziffer, M.E., Snaith, H.J., Ginger, D.S.: Impact of microstructure on local carrier lifetime in perovskite solar cells. *Science* **348**(6235), 683–686 (2015) <https://doi.org/10.1126/science.aaa5333> . Accessed 2024-02-29
- [9] Park, N.-G., Grätzel, M., Miyasaka, T., Zhu, K., Emery, K.: Towards stable and commercially available perovskite solar cells. *Nature Energy* **1**(11), 16152 (2016) <https://doi.org/10.1038/nenergy.2016.152> . Accessed 2024-02-29
- [10] Udayabhaskararao, T., Kazes, M., Houben, L., Lin, H., Oron, D.: Nucleation, Growth, and Structural Transformations of Perovskite Nanocrystals. *Chemistry of Materials* **29**(3), 1302–1308 (2017) <https://doi.org/10.1021/acs.chemmater.6b04841> . Accessed 2022-10-17
- [11] Peng, L., Dutta, A., Xie, R., Yang, W., Pradhan, N.: Dot–Wire–Platelet–Cube: Step Growth and Structural Transformations in CsPbBr_3 Perovskite Nanocrystals. *ACS Energy Letters* **3**(8), 2014–2020 (2018) <https://doi.org/10.1021/acsenergylett.8b01037> . Accessed 2022-10-17
- [12] Correa-Baena, J.-P., Luo, Y., Brenner, T.M., Snaider, J., Sun, S., Li, X., Jensen, M.A., Hartono, N.T.P., Nienhaus, L., Wieghold, S., Poindexter, J.R., Wang, S.,

- Meng, Y.S., Wang, T., Lai, B., Holt, M.V., Cai, Z., Bawendi, M.G., Huang, L., Buonassisi, T., Fenning, D.P.: Homogenized halides and alkali cation segregation in alloyed organic-inorganic perovskites. *Science* **363**(6427), 627–631 (2019) <https://doi.org/10.1126/science.aah5065> . Accessed 2024-02-29
- [13] Jena, A.K., Kulkarni, A., Miyasaka, T.: Halide Perovskite Photovoltaics: Background, Status, and Future Prospects. *Chemical Reviews* **119**(5), 3036–3103 (2019) <https://doi.org/10.1021/acs.chemrev.8b00539> . Accessed 2024-02-29
- [14] Kosar, S., Winchester, A.J., Doherty, T.A.S., Macpherson, S., Petoukhoff, C.E., Frohma, K., Anaya, M., Chan, N.S., Madéo, J., Man, M.K.L., Stranks, S.D., Dani, K.M.: Unraveling the varied nature and roles of defects in hybrid halide perovskites with time-resolved photoemission electron microscopy. *Energy & Environmental Science* **14**(12), 6320–6328 (2021) <https://doi.org/10.1039/D1EE02055B> . Accessed 2024-02-29
- [15] Akkerman, Q.A., Rainò, G., Kovalenko, M.V., Manna, L.: Genesis, challenges and opportunities for colloidal lead halide perovskite nanocrystals. *Nature Materials* **17**(5), 394–405 (2018) <https://doi.org/10.1038/s41563-018-0018-4> . Accessed 2022-10-17
- [16] Kim, Y., Kim, J.S., Lee, T.: Strategies to Improve Luminescence Efficiency of Metal-Halide Perovskites and Light-Emitting Diodes. *Advanced Materials* **31**(47), 1804595 (2019) <https://doi.org/10.1002/adma.201804595> . Accessed 2022-10-15
- [17] Xue, J., Wang, R., Yang, Y.: The surface of halide perovskites from nano to bulk. *Nature Reviews Materials* **5**(11), 809–827 (2020) <https://doi.org/10.1038/s41578-020-0221-1> . Accessed 2022-10-16
- [18] Li, W., Rothmann, M.U., Zhu, Y., Chen, W., Yang, C., Yuan, Y., Choo, Y.Y., Wen, X., Cheng, Y.-B., Bach, U., Etheridge, J.: The critical role of composition-dependent intragrain planar defects in the performance of $\text{MA}_{1-x}\text{FA}_x\text{PbI}_3$ perovskite solar cells. *Nature Energy* **6**(6), 624–632 (2021) <https://doi.org/10.1038/s41560-021-00830-9> . Accessed 2022-10-16
- [19] Dey, A., Ye, J., De, A., Debroye, E., Ha, S.K., Bladt, E., Kshirsagar, A.S., Wang, Z., Yin, J., Wang, Y., Quan, L.N., Yan, F., Gao, M., Li, X., Shamsi, J., Debnath, T., Cao, M., Scheel, M.A., Kumar, S., Steele, J.A., Gerhard, M., Chouhan, L., Xu, K., Wu, X.-g., Li, Y., Zhang, Y., Dutta, A., Han, C., Vincon, I., Rogach, A.L., Nag, A., Samanta, A., Korgel, B.A., Shih, C.-J., Gamelin, D.R., Son, D.H., Zeng, H., Zhong, H., Sun, H., Demir, H.V., Scheblykin, I.G., Mora-Seró, I., Stolarczyk, J.K., Zhang, J.Z., Feldmann, J., Hofkens, J., Luther, J.M., Pérez-Prieto, J., Li, L., Manna, L., Bodnarchuk, M.I., Kovalenko, M.V., Roeffaers, M.B.J., Pradhan, N., Mohammed, O.F., Bakr, O.M., Yang, P., Müller-Buschbaum, P., Kamat, P.V., Bao, Q., Zhang, Q., Krahne, R., Galian, R.E., Stranks, S.D., Bals, S., Biju, V., Tisdale, W.A., Yan, Y., Hoye, R.L.Z., Polavarapu, L.:

State of the Art and Prospects for Halide Perovskite Nanocrystals. ACS Nano **15**(7), 10775–10981 (2021) <https://doi.org/10.1021/acsnano.0c08903> . Accessed 2022-10-12

- [20] Arora, N., Greco, A., Meloni, S., Hinderhofer, A., Mattoni, A., Rothlisberger, U., Hagenlocher, J., Caddeo, C., Zakeeruddin, S.M., Schreiber, F., Graetzel, M., Friend, R.H., Dar, M.I.: Kinetics and energetics of metal halide perovskite conversion reactions at the nanoscale. Communications Materials **3**(1), 22 (2022) <https://doi.org/10.1038/s43246-022-00239-1> . Accessed 2024-02-29
- [21] Han, T.-H., Jang, K.Y., Dong, Y., Friend, R.H., Sargent, E.H., Lee, T.-W.: A roadmap for the commercialization of perovskite light emitters. Nature Reviews Materials **7**(10), 757–777 (2022) <https://doi.org/10.1038/s41578-022-00459-4> . Accessed 2022-10-15
- [22] Dong, S., Hu, Z., Wei, P., Han, J., Wang, Z., Liu, J., Su, B., Zhao, D., Liu, Y.: All-Inorganic Perovskite Single-Crystal Photoelectric Anisotropy. Advanced Materials **34**(37), 2204342 (2022) <https://doi.org/10.1002/adma.202204342> . Accessed 2022-10-13
- [23] Ma, C., Grätzel, M., Park, N.-G.: Facet Engineering for Stable, Efficient Perovskite Solar Cells. ACS Energy Letters **7**(9), 3120–3128 (2022) <https://doi.org/10.1021/acsenergylett.2c01623> . Accessed 2022-10-13
- [24] Park, J., Kim, J., Yun, H.-S., Paik, M.J., Noh, E., Mun, H.J., Kim, M.G., Shin, T.J., Seok, S.I.: Controlled growth of perovskite layers with volatile alkylammonium chlorides. Nature **616**(7958), 724–730 (2023) <https://doi.org/10.1038/s41586-023-05825-y> . Accessed 2024-02-29
- [25] Wells, H.L.: Über die Cäsium- und Kalium-Bleihalogenide. Zeitschrift für anorganische Chemie **3**(1), 195–210 (1893) <https://doi.org/10.1002/zaac.18930030124> . Accessed 2022-10-12
- [26] Kim, Y.-H., Cho, H., Lee, T.-W.: Metal halide perovskite light emitters. Proceedings of the National Academy of Sciences **113**(42), 11694–11702 (2016) <https://doi.org/10.1073/pnas.1607471113> . Accessed 2022-10-15
- [27] Lin, K., Xing, J., Quan, L.N., Arquer, F.P.G., Gong, X., Lu, J., Xie, L., Zhao, W., Zhang, D., Yan, C., Li, W., Liu, X., Lu, Y., Kirman, J., Sargent, E.H., Xiong, Q., Wei, Z.: Perovskite light-emitting diodes with external quantum efficiency exceeding 20 per cent. Nature **562**(7726), 245–248 (2018) <https://doi.org/10.1038/s41586-018-0575-3> . Accessed 2022-10-16
- [28] Utzat, H., Sun, W., Kaplan, A.E.K., Krieg, F., Ginterseder, M., Spokoyny, B., Klein, N.D., Shulenberger, K.E., Perkinson, C.F., Kovalenko, M.V., Bawendi, M.G.: Coherent single-photon emission from colloidal lead halide perovskite quantum dots. Science **363**(6431), 1068–1072 (2019) <https://doi.org/10.1126/>

science.aau7392 . Accessed 2022-10-15

- [29] Hassan, Y., Park, J.H., Crawford, M.L., Sadhanala, A., Lee, J., Sadighian, J.C., Mosconi, E., Shivanna, R., Radicchi, E., Jeong, M., Yang, C., Choi, H., Park, S.H., Song, M.H., De Angelis, F., Wong, C.Y., Friend, R.H., Lee, B.R., Snaith, H.J.: Ligand-engineered bandgap stability in mixed-halide perovskite LEDs. *Nature* **591**(7848), 72–77 (2021) <https://doi.org/10.1038/s41586-021-03217-8> . Accessed 2022-10-15
- [30] Helio Display (2023). <https://www.heliodisplaymaterials.com/> Accessed 2022-10-15
- [31] <https://avantama.com/> Accessed 2022-10-15
- [32] Stoumpos, C.C., Malliakas, C.D., Peters, J.A., Liu, Z., Sebastian, M., Im, J., Chasapis, T.C., Wibowo, A.C., Chung, D.Y., Freeman, A.J., Wessels, B.W., Kanatzidis, M.G.: Crystal Growth of the Perovskite Semiconductor CsPbBr₃: A New Material for High-Energy Radiation Detection. *Crystal Growth & Design* **13**(7), 2722–2727 (2013) <https://doi.org/10.1021/cg400645t> . Accessed 2022-10-13
- [33] Zhu, X., Lin, Y., San Martin, J., Sun, Y., Zhu, D., Yan, Y.: Lead halide perovskites for photocatalytic organic synthesis. *Nature Communications* **10**(1), 2843 (2019) <https://doi.org/10.1038/s41467-019-10634-x> . Accessed 2022-10-16
- [34] DuBose, J.T., Kamat, P.V.: Efficacy of Perovskite Photocatalysis: Challenges to Overcome. *ACS Energy Letters* **7**(6), 1994–2011 (2022) <https://doi.org/10.1021/acsenergylett.2c00765> . Accessed 2022-10-13
- [35] DuBose, J.T., Kamat, P.V.: Energy Versus Electron Transfer: Managing Excited-State Interactions in Perovskite Nanocrystal–Molecular Hybrids: Focus Review. *Chemical Reviews* **122**(15), 12475–12494 (2022) <https://doi.org/10.1021/acs.chemrev.2c00172> . Accessed 2022-10-13
- [36] Duan, J., Zhao, Y., He, B., Tang, Q.: High-Purity Inorganic Perovskite Films for Solar Cells with 9.72 % Efficiency. *Angewandte Chemie International Edition* **57**(14), 3787–3791 (2018) <https://doi.org/10.1002/anie.201800019> . Accessed 2023-07-07
- [37] Li, T., Xu, J., Lin, R., Teale, S., Li, H., Liu, Z., Duan, C., Zhao, Q., Xiao, K., Wu, P., Chen, B., Jiang, S., Xiong, S., Luo, H., Wan, S., Li, L., Bao, Q., Tian, Y., Gao, X., Xie, J., Sargent, E.H., Tan, H.: Inorganic wide-bandgap perovskite subcells with dipole bridge for all-perovskite tandems. *Nature Energy* (2023) <https://doi.org/10.1038/s41560-023-01250-7> . Accessed 2023-06-15
- [38] Wang, Z., Zeng, L., Zhu, T., Chen, H., Chen, B., Kubicki, D.J., Balvanz, A., Li, C., Maxwell, A., Ugur, E., Dos Reis, R., Cheng, M., Yang, G., Subedi, B., Luo,

- D., Hu, J., Wang, J., Teale, S., Mahesh, S., Wang, S., Hu, S., Jung, E.D., Wei, M., Park, S.M., Grater, L., Aydin, E., Song, Z., Podraza, N.J., Lu, Z.-H., Huang, J., Dravid, V.P., De Wolf, S., Yan, Y., Grätzel, M., Kanatzidis, M.G., Sargent, E.H.: Suppressed phase segregation for triple-junction perovskite solar cells. *Nature* **618**(7963), 74–79 (2023) <https://doi.org/10.1038/s41586-023-06006-7> . Accessed 2023-06-16
- [39] Rainò, G., Becker, M.A., Bodnarchuk, M.I., Mahrt, R.F., Kovalenko, M.V., Stöferle, T.: Superfluorescence from lead halide perovskite quantum dot superlattices. *Nature* **563**(7733), 671–675 (2018) <https://doi.org/10.1038/s41586-018-0683-0> . Accessed 2022-08-08
- [40] Cherniukh, I., Rainò, G., Stöferle, T., Burian, M., Travasset, A., Naumenko, D., Amenitsch, H., Erni, R., Mahrt, R.F., Bodnarchuk, M.I., Kovalenko, M.V.: Perovskite-type superlattices from lead halide perovskite nanocubes. *Nature* **593**(7860), 535–542 (2021) <https://doi.org/10.1038/s41586-021-03492-5> . Accessed 2022-08-08
- [41] Bilioglu, M., Findik, G., Mendes, J., Seyitliyev, D., Lei, L., Dong, Q., Mehta, Y., Temnov, V.V., So, F., Gundogdu, K.: Room-temperature superfluorescence in hybrid perovskites and its origins. *Nature Photonics* **16**(4), 324–329 (2022) <https://doi.org/10.1038/s41566-022-00974-4> . Accessed 2022-08-08
- [42] Dicke, R.H.: Coherence in Spontaneous Radiation Processes. *Physical Review* **93**(1), 99–110 (1954) <https://doi.org/10.1103/PhysRev.93.99> . Accessed 2022-08-08
- [43] Bonifacio, R., Lugiato, L.A.: Cooperative radiation processes in two-level systems: Superfluorescence. *Physical Review A* **11**(5), 1507–1521 (1975) <https://doi.org/10.1103/PhysRevA.11.1507> . Accessed 2022-08-08
- [44] Shcherbakov-Wu, W., Saris, S., Sheehan, T., Wong, N.N., Powers, E.R., Krieg, F., Kovalenko, M.V., Willard, A.P., Tisdale, W.A.: Persistent Enhancement of Exciton Diffusivity in CsPbBr₃ Nanocrystal Solids. *arXiv*. arXiv:2209.14412 [cond-mat] (2022). <http://arxiv.org/abs/2209.14412> Accessed 2022-10-17
- [45] Duan, L., Zhang, H., Eickemeyer, F.T., Gao, J., Zakeeruddin, S.M., Grätzel, M., Luo, J.: CsPbBr₃ Quantum Dots-Sensitized Mesoporous TiO₂ Electron Transport Layers for High-Efficiency Perovskite Solar Cells. *Solar RRL* **7**(11), 2300072 (2023) <https://doi.org/10.1002/solr.202300072> . Accessed 2023-07-12
- [46] Lin, R., Wang, Y., Lu, Q., Tang, B., Li, J., Gao, H., Gao, Y., Li, H., Ding, C., Wen, J., Wu, P., Liu, C., Zhao, S., Xiao, K., Liu, Z., Ma, C., Deng, Y., Li, L., Fan, F., Tan, H.: All-perovskite tandem solar cells with 3D/3D bilayer perovskite heterojunction. *Nature* (2023) <https://doi.org/10.1038/s41586-023-06278-z> . Accessed 2023-06-15

- [47] Interactive Best Research-Cell Efficiency Chart. <https://www.nrel.gov/pv/interactive-cell-efficiency.html> Accessed 2024-05-05
- [48] Chin, X.Y., Turkay, D., Steele, J.A., Tabean, S., Eswara, S., Mensi, M., Fiala, P., Wolff, C.M., Paracchino, A., Artuk, K., Jacobs, D., Guesnay, Q., Sahli, F., Andreatta, G., Boccard, M., Jeangros, Q., Ballif, C.: Interface passivation for 31.25%-efficient perovskite/silicon tandem solar cells. *Science* **381**(6653), 59–63 (2023) <https://doi.org/10.1126/science.adg0091> . Accessed 2023-07-12
- [49] De Wolf, S., Aydin, E.: Tandems have the power. *Science* **381**(6653), 30–31 (2023) <https://doi.org/10.1126/science.adg0091> . Accessed 2023-07-12
- [50] Koscher, B.A., Swabedek, J.K., Bronstein, N.D., Alivisatos, A.P.: Essentially Trap-Free CsPbBr₃ Colloidal Nanocrystals by Postsynthetic Thiocyanate Surface Treatment. *Journal of the American Chemical Society* **139**(19), 6566–6569 (2017) <https://doi.org/10.1021/jacs.7b02817> . Accessed 2022-10-15
- [51] Akkerman, Q.A., Gandini, M., Di Stasio, F., Rastogi, P., Palazon, F., Bertoni, G., Ball, J.M., Prato, M., Petrozza, A., Manna, L.: Strongly emissive perovskite nanocrystal inks for high-voltage solar cells. *Nature Energy* **2**(2), 16194 (2017) <https://doi.org/10.1038/nenergy.2016.194> . Accessed 2022-10-17
- [52] Peng, L., Dutta, S.K., Mondal, D., Hudait, B., Shyamal, S., Xie, R., Mahadevan, P., Pradhan, N.: Arm Growth and Facet Modulation in Perovskite Nanocrystals. *Journal of the American Chemical Society* **141**(40), 16160–16168 (2019) <https://doi.org/10.1021/jacs.9b09157> . Accessed 2022-10-17
- [53] Gualdrón-Reyes, A.F., Yoon, S.J., Barea, E.M., Agouram, S., Muñoz-Sanjosé, V., Meléndez, A.M., Niño-Gómez, M.E., Mora-Seró, I.: Controlling the Phase Segregation in Mixed Halide Perovskites through Nanocrystal Size. *ACS Energy Letters* **4**(1), 54–62 (2019) <https://doi.org/10.1021/acsenergylett.8b02207> . Accessed 2022-10-15
- [54] Wu, T., Li, J., Zou, Y., Xu, H., Wen, K., Wan, S., Bai, S., Song, T., McLeod, J.A., Duhm, S., Gao, F., Sun, B.: High-Performance Perovskite Light-Emitting Diode with Enhanced Operational Stability Using Lithium Halide Passivation. *Angewandte Chemie International Edition* **59**(10), 4099–4105 (2020) <https://doi.org/10.1002/anie.201914000> . Accessed 2022-10-15
- [55] Protesescu, L., Yakunin, S., Bodnarchuk, M.I., Krieg, F., Caputo, R., Hendon, C.H., Yang, R.X., Walsh, A., Kovalenko, M.V.: Nanocrystals of Cesium Lead Halide Perovskites (CsPbX₃, X = Cl, Br, and I): Novel Optoelectronic Materials Showing Bright Emission with Wide Color Gamut. *Nano Letters* **15**(6), 3692–3696 (2015) <https://doi.org/10.1021/nl5048779> . Accessed 2022-10-12
- [56] Zhang, F., Zhong, H., Chen, C., Wu, X.-g., Hu, X., Huang, H., Han, J., Zou, B., Dong, Y.: Brightly Luminescent and Color-Tunable Colloidal CH₃NH₃PbX₃

(X = Br, I, Cl) Quantum Dots: Potential Alternatives for Display Technology. ACS Nano **9**(4), 4533–4542 (2015) <https://doi.org/10.1021/acsnano.5b01154> . Accessed 2022-10-12

- [57] Li, X., Wu, Y., Zhang, S., Cai, B., Gu, Y., Song, J., Zeng, H.: CsPbX₃ Quantum Dots for Lighting and Displays: Room-Temperature Synthesis, Photoluminescence Superiorities, Underlying Origins and White Light-Emitting Diodes. Advanced Functional Materials **26**(15), 2435–2445 (2016) <https://doi.org/10.1002/adfm.201600109> . Accessed 2022-10-13
- [58] Pan, A., He, B., Fan, X., Liu, Z., Urban, J.J., Alivisatos, A.P., He, L., Liu, Y.: Insight into the Ligand-Mediated Synthesis of Colloidal CsPbBr₃ Perovskite Nanocrystals: The Role of Organic Acid, Base, and Cesium Precursors. ACS Nano **10**(8), 7943–7954 (2016) <https://doi.org/10.1021/acsnano.6b03863> . Accessed 2022-10-12
- [59] Sichert, J.A., Tong, Y., Mutz, N., Vollmer, M., Fischer, S., Milowska, K.Z., García Cortadella, R., Nickel, B., Cardenas-Daw, C., Stolarczyk, J.K., Urban, A.S., Feldmann, J.: Quantum Size Effect in Organometal Halide Perovskite Nanoplatelets. Nano Letters **15**(10), 6521–6527 (2015) <https://doi.org/10.1021/acs.nanolett.5b02985> . Accessed 2022-10-12
- [60] Liu, F., Zhang, Y., Ding, C., Kobayashi, S., Izuishi, T., Nakazawa, N., Toyoda, T., Ohta, T., Hayase, S., Minemoto, T., Yoshino, K., Dai, S., Shen, Q.: Highly Luminescent Phase-Stable CsPbI₃ Perovskite Quantum Dots Achieving Near 100% Absolute Photoluminescence Quantum Yield. ACS Nano **11**(10), 10373–10383 (2017) <https://doi.org/10.1021/acsnano.7b05442> . Accessed 2022-10-13
- [61] Wu, L., Zhong, Q., Yang, D., Chen, M., Hu, H., Pan, Q., Liu, H., Cao, M., Xu, Y., Sun, B., Zhang, Q.: Improving the Stability and Size Tunability of Cesium Lead Halide Perovskite Nanocrystals Using Trioctylphosphine Oxide as the Capping Ligand. Langmuir **33**(44), 12689–12696 (2017) <https://doi.org/10.1021/acs.langmuir.7b02963> . Accessed 2022-10-13
- [62] Barker, A.J., Sadhanala, A., Deschler, F., Gandini, M., Senanayak, S.P., Pearce, P.M., Mosconi, E., Pearson, A.J., Wu, Y., Srimath Kandada, A.R., Leijtens, T., De Angelis, F., Dutton, S.E., Petrozza, A., Friend, R.H.: Defect-Assisted Photoinduced Halide Segregation in Mixed-Halide Perovskite Thin Films. ACS Energy Letters **2**(6), 1416–1424 (2017) <https://doi.org/10.1021/acsenergylett.7b00282> . Accessed 2022-10-15
- [63] Lai, M., Obliger, A., Lu, D., Kley, C.S., Bischak, C.G., Kong, Q., Lei, T., Dou, L., Ginsberg, N.S., Limmer, D.T., Yang, P.: Intrinsic anion diffusivity in lead halide perovskites is facilitated by a soft lattice. Proceedings of the National Academy of Sciences **115**(47), 11929–11934 (2018) <https://doi.org/10.1073/pnas.1812718115> . Accessed 2022-10-13

- [64] Zhang, H., Fu, X., Tang, Y., Wang, H., Zhang, C., Yu, W.W., Wang, X., Zhang, Y., Xiao, M.: Phase segregation due to ion migration in all-inorganic mixed-halide perovskite nanocrystals. *Nature Communications* **10**(1), 1088 (2019) <https://doi.org/10.1038/s41467-019-09047-7> . Accessed 2022-10-15
- [65] Song, J., Cui, Q., Li, J., Xu, J., Wang, Y., Xu, L., Xue, J., Dong, Y., Tian, T., Sun, H., Zeng, H.: Ultralarge All-Inorganic Perovskite Bulk Single Crystal for High-Performance Visible-Infrared Dual-Modal Photodetectors. *Advanced Optical Materials* **5**(12), 1700157 (2017) <https://doi.org/10.1002/adom.201700157> . Accessed 2022-10-13
- [66] He, Y., Matei, L., Jung, H.J., McCall, K.M., Chen, M., Stoumpos, C.C., Liu, Z., Peters, J.A., Chung, D.Y., Wessels, B.W., Wasielewski, M.R., Dravid, V.P., Burger, A., Kanatzidis, M.G.: High spectral resolution of gamma-rays at room temperature by perovskite CsPbBr₃ single crystals. *Nature Communications* **9**(1), 1609 (2018) <https://doi.org/10.1038/s41467-018-04073-3> . Accessed 2022-10-13
- [67] Wang, B., Zhang, C., Zheng, W., Zhang, Q., Wan, Q., Kong, L., Li, L.: Synthesis of lead halide perovskite nanocrystals by melt crystallization in halide salts. *Chemical Communications* **56**(76), 11291–11294 (2020) <https://doi.org/10.1039/D0CC04020G> . Accessed 2022-10-13
- [68] Liu, Z., Sinatra, L., Lutfullin, M., Ivanov, Y.P., Divitini, G., De Trizio, L., Manna, L.: One Hundred-Nanometer-Sized CsPbBr₃/m-SiO₂ Composites Prepared via Molten-Salts Synthesis are Optimal Green Phosphors for LCD Display Devices. *Advanced Energy Materials*, 2201948 (2022) <https://doi.org/10.1002/aenm.202201948> . Accessed 2022-10-13
- [69] Maceiczyk, R.M., Dümbgen, K., Lignos, I., Protesescu, L., Kovalenko, M.V., deMello, A.J.: Microfluidic Reactors Provide Preparative and Mechanistic Insights into the Synthesis of Formamidinium Lead Halide Perovskite Nanocrystals. *Chemistry of Materials* **29**(19), 8433–8439 (2017) <https://doi.org/10.1021/acs.chemmater.7b02998> . Accessed 2022-10-15
- [70] Wu, Y., Li, X., Zeng, H.: Highly Luminescent and Stable Halide Perovskite Nanocrystals. *ACS Energy Letters* **4**(3), 673–681 (2019) <https://doi.org/10.1021/acsenergylett.8b02100> . Accessed 2022-10-13
- [71] Shamsi, J., Urban, A.S., Imran, M., De Trizio, L., Manna, L.: Metal Halide Perovskite Nanocrystals: Synthesis, Post-Synthesis Modifications, and Their Optical Properties. *Chemical Reviews* **119**(5), 3296–3348 (2019) <https://doi.org/10.1021/acs.chemrev.8b00644> . Accessed 2022-10-15
- [72] Burlakov, V.M., Hassan, Y., Danaie, M., Snaith, H.J., Goriely, A.: Competitive Nucleation Mechanism for CsPbBr₃ Perovskite Nanoplatelet Growth. *The Journal of Physical Chemistry Letters* **11**(16), 6535–6543 (2020) <https://doi.org/10.1021/acs.jpclett.0c00832>

[//doi.org/10.1021/acs.jpcllett.0c01794](https://doi.org/10.1021/acs.jpcllett.0c01794) . Accessed 2022-10-17

- [73] Kipkorir, A., DuBose, J., Cho, J., Kamat, P.V.: CsPbBr₃–CdS heterostructure: stabilizing perovskite nanocrystals for photocatalysis. *Chemical Science* **12**(44), 14815–14825 (2021) <https://doi.org/10.1039/D1SC04305F> . Accessed 2022-10-13
- [74] Pradhan, N.: Why Do Perovskite Nanocrystals Form Nanocubes and How Can Their Facets Be Tuned? A Perspective from Synthetic Prospects. *ACS Energy Letters* **6**(1), 92–99 (2021) <https://doi.org/10.1021/acsenergylett.0c02099> . Accessed 2022-10-13
- [75] Baek, K.-Y., Lee, W., Lee, J., Kim, J., Ahn, H., Kim, J.I., Kim, J., Lim, H., Shin, J., Ko, Y.-J., Lee, H.-D., Friend, R.H., Lee, T.-W., Lee, J., Kang, K., Lee, T.: Mechanochemistry-driven engineering of 0D/3D heterostructure for designing highly luminescent Cs–Pb–Br perovskites. *Nature Communications* **13**(1), 4263 (2022) <https://doi.org/10.1038/s41467-022-31924-x> . Accessed 2022-10-15
- [76] Si, J., Liu, Y., He, Z., Du, H., Du, K., Chen, D., Li, J., Xu, M., Tian, H., He, H., Di, D., Lin, C., Cheng, Y., Wang, J., Jin, Y.: Efficient and High-Color-Purity Light-Emitting Diodes Based on *In Situ* Grown Films of CsPbX₃ (X = Br, I) Nanoplates with Controlled Thicknesses. *ACS Nano* **11**(11), 11100–11107 (2017) <https://doi.org/10.1021/acsnano.7b05191> . Accessed 2022-10-15
- [77] Das, R., Patra, A., Dutta, S.K., Shyamal, S., Pradhan, N.: Facets-Directed Epitaxially Grown Lead Halide Perovskite-Sulfobromide Nanocrystal Heterostructures and Their Improved Photocatalytic Activity. *Journal of the American Chemical Society* **144**(40), 18629–18641 (2022) <https://doi.org/10.1021/jacs.2c08639> . Accessed 2022-10-17
- [78] <https://quantum-solutions.com/> Accessed 2022-10-15
- [79] <https://peroled.com/> Accessed 2022-10-15
- [80] <https://nanolumi.com/> Accessed 2022-10-15
- [81] <http://www.zhijingtech.cn/> Accessed 2022-10-15
- [82] Zhang, B., Altamura, D., Caliandro, R., Giannini, C., Peng, L., De Trizio, L., Manna, L.: Stable CsPbBr₃ Nanoclusters Feature a Disk-like Shape and a Distorted Orthorhombic Structure. *Journal of the American Chemical Society* **144**(11), 5059–5066 (2022) <https://doi.org/10.1021/jacs.1c13544> . Accessed 2022-10-17
- [83] Akkerman, Q.A., Nguyen, T.P.T., Boehme, S.C., Montanarella, F., Dirin, D.N., Wechsler, P., Beiglböck, F., Rainò, G., Erni, R., Katan, C., Even, J., Kovalenko, M.V.: Controlling the nucleation and growth kinetics of lead halide perovskite

quantum dots. *Science* **377**(6613), 1406–1412 (2022) <https://doi.org/10.1126/science.abq3616> . Accessed 2022-10-15

- [84] Nakamuro, T., Sakakibara, M., Nada, H., Harano, K., Nakamura, E.: Capturing the Moment of Emergence of Crystal Nucleus from Disorder. *Journal of the American Chemical Society* **143**(4), 1763–1767 (2021) <https://doi.org/10.1021/jacs.0c12100> . Accessed 2024-02-29
- [85] Chevalier, O.J.G.L., Nakamuro, T., Sato, W., Miyashita, S., Chiba, T., Kido, J., Shang, R., Nakamura, E.: Precision Synthesis and Atomistic Analysis of Deep-Blue Cubic Quantum Dots Made via Self-Organization. *Journal of the American Chemical Society* **144**(46), 21146–21156 (2022) <https://doi.org/10.1021/jacs.2c08227> . Accessed 2024-02-29
- [86] Wolde, P., Ruiz-Montero, M.J., Frenkel, D.: Numerical calculation of the rate of crystal nucleation in a Lennard-Jones system at moderate undercooling. *The Journal of Chemical Physics* **104**(24), 9932–9947 (1996) <https://doi.org/10.1063/1.471721> . Accessed 2022-10-17
- [87] Wolde, P.R.t., Frenkel, D.: Enhancement of Protein Crystal Nucleation by Critical Density Fluctuations. *Science* **277**(5334), 1975–1978 (1997) <https://doi.org/10.1126/science.277.5334.1975> . Accessed 2022-10-17
- [88] Cacciuto, A., Auer, S., Frenkel, D.: Onset of heterogeneous crystal nucleation in colloidal suspensions. *Nature* **428**(6981), 404–406 (2004) <https://doi.org/10.1038/nature02397> . Accessed 2022-10-17
- [89] Piana, S., Reyhani, M., Gale, J.D.: Simulating micrometre-scale crystal growth from solution. *Nature* **438**(7064), 70–73 (2005) <https://doi.org/10.1038/nature04173> . Accessed 2022-10-17
- [90] Piana, S., Gale, J.D.: Understanding the Barriers to Crystal Growth: Dynamical Simulation of the Dissolution and Growth of Urea from Aqueous Solution. *Journal of the American Chemical Society* **127**(6), 1975–1982 (2005) <https://doi.org/10.1021/ja0433951> . Accessed 2022-10-17
- [91] Valeriani, C., Sanz, E., Frenkel, D.: Rate of homogeneous crystal nucleation in molten NaCl. *The Journal of Chemical Physics* **122**(19), 194501 (2005) <https://doi.org/10.1063/1.1896348> . Accessed 2023-07-18
- [92] Kawasaki, T., Tanaka, H.: Formation of a crystal nucleus from liquid. *Proceedings of the National Academy of Sciences* **107**(32), 14036–14041 (2010) <https://doi.org/10.1073/pnas.1001040107> . Accessed 2022-10-17
- [93] Van Meel, J.A., Sear, R.P., Frenkel, D.: Design Principles for Broad-Spectrum Protein-Crystal Nucleants with Nanoscale Pits. *Physical Review Letters* **105**(20), 205501 (2010) <https://doi.org/10.1103/PhysRevLett.105.205501> .

Accessed 2024-05-17

- [94] Anwar, J., Zahn, D.: Uncovering Molecular Processes in Crystal Nucleation and Growth by Using Molecular Simulation. *Angewandte Chemie International Edition* **50**(9), 1996–2013 (2011) <https://doi.org/10.1002/anie.201000463> . Accessed 2022-10-17
- [95] Lechner, W., Dellago, C., Bolhuis, P.G.: Role of the Prestructured Surface Cloud in Crystal Nucleation. *Physical Review Letters* **106**(8), 085701 (2011) <https://doi.org/10.1103/PhysRevLett.106.085701> . Accessed 2024-02-29
- [96] Chakraborty, D., Patey, G.N.: Evidence that crystal nucleation in aqueous NaCl solution Occurs by the two-step mechanism. *Chemical Physics Letters* **587**, 25–29 (2013) <https://doi.org/10.1016/j.cplett.2013.09.054> . Accessed 2022-10-17
- [97] Zimmermann, N.E.R., Vorselaars, B., Quigley, D., Peters, B.: Nucleation of NaCl from Aqueous Solution: Critical Sizes, Ion-Attachment Kinetics, and Rates. *Journal of the American Chemical Society* **137**(41), 13352–13361 (2015) <https://doi.org/10.1021/jacs.5b08098> . Accessed 2022-10-17
- [98] Espinosa, J.R., Vega, C., Valeriani, C., Sanz, E.: The crystal-fluid interfacial free energy and nucleation rate of NaCl from different simulation methods. *The Journal of Chemical Physics* **142**(19), 194709 (2015) <https://doi.org/10.1063/1.4921185> . Accessed 2022-10-17
- [99] Salvalaglio, M., Perego, C., Giberti, F., Mazzotti, M., Parrinello, M.: Molecular-dynamics simulations of urea nucleation from aqueous solution. *Proceedings of the National Academy of Sciences* **112**(1) (2015) <https://doi.org/10.1073/pnas.1421192111> . Accessed 2024-02-29
- [100] Espinosa, J.R., Vega, C., Valeriani, C., Sanz, E.: Seeding approach to crystal nucleation. *The Journal of Chemical Physics* **144**(3), 034501 (2016) <https://doi.org/10.1063/1.4939641> . Accessed 2022-10-17
- [101] Jungblut, S., Dellago, C.: Pathways to self-organization: Crystallization via nucleation and growth. *The European Physical Journal E* **39**(8), 77 (2016) <https://doi.org/10.1140/epje/i2016-16077-6> . Accessed 2022-10-17
- [102] Anderson, M.W., Gebbie-Rayet, J.T., Hill, A.R., Farida, N., Attfield, M.P., Cubillas, P., Blatov, V.A., Proserpio, D.M., Akporiaye, D., Arstad, B., Gale, J.D.: Predicting crystal growth via a unified kinetic three-dimensional partition model. *Nature* **544**(7651), 456–459 (2017) <https://doi.org/10.1038/nature21684> . Accessed 2022-10-17
- [103] Shibuta, Y., Sakane, S., Miyoshi, E., Okita, S., Takaki, T., Ohno, M.: Heterogeneity in homogeneous nucleation from billion-atom molecular dynamics simulation of solidification of pure metal. *Nature Communications* **8**(1), 10

(2017) <https://doi.org/10.1038/s41467-017-00017-5> . Accessed 2022-10-17

- [104] Elm, J., Kubečka, J., Besel, V., Jääskeläinen, M.J., Halonen, R., Kurtén, T., Vehkamäki, H.: Modeling the formation and growth of atmospheric molecular clusters: A review. *Journal of Aerosol Science* **149**, 105621 (2020) <https://doi.org/10.1016/j.jaerosci.2020.105621> . Accessed 2023-06-18
- [105] Arjun, Berendsen, T.A., Bolhuis, P.G.: Unbiased atomistic insight in the competing nucleation mechanisms of methane hydrates. *Proceedings of the National Academy of Sciences* **116**(39), 19305–19310 (2019) <https://doi.org/10.1073/pnas.1906502116> . Accessed 2024-02-29
- [106] Ahlawat, P., Dar, M.I., Piaggi, P., Grätzel, M., Parrinello, M., Rothlisberger, U.: Atomistic Mechanism of the Nucleation of Methylammonium Lead Iodide Perovskite from Solution. *Chemistry of Materials* **32**(1), 529–536 (2020) <https://doi.org/10.1021/acs.chemmater.9b04259> . Accessed 2024-05-16
- [107] Lu, H., Liu, Y., Ahlawat, P., Mishra, A., Tress, W.R., Eickemeyer, F.T., Yang, Y., Fu, F., Wang, Z., Avalos, C.E., Carlsen, B.I., Agarwalla, A., Zhang, X., Li, X., Zhan, Y., Zakeeruddin, S.M., Emsley, L., Rothlisberger, U., Zheng, L., Hagfeldt, A., Grätzel, M.: Vapor-assisted deposition of highly efficient, stable black-phase FAPbI₃ perovskite solar cells. *Science* **370**(6512), 8985 (2020) <https://doi.org/10.1126/science.abb8985> . Accessed 2024-05-16
- [108] Ahlawat, P., Hinderhofer, A., Alharbi, E.A., Lu, H., Ummadisingu, A., Niu, H., Invernizzi, M., Zakeeruddin, S.M., Dar, M.I., Schreiber, F., Hagfeldt, A., Grätzel, M., Rothlisberger, U., Parrinello, M.: A combined molecular dynamics and experimental study of two-step process enabling low-temperature formation of phase-pure α-FAPbI₃. *Science Advances* **7**(17), 3326 (2021) <https://doi.org/10.1126/sciadv.abe3326> . Accessed 2023-07-16
- [109] Ahlawat, P.: Crystallization of FAPbI3: Polytypes and stacking faults. *The Journal of Chemical Physics* **159**(15), 151102 (2023) <https://doi.org/10.1063/5.0165285> . Accessed 2024-05-17
- [110] Ahlawat, P.: Size dependent solid-solid crystallization of halide perovskites. arXiv. arXiv:2404.05644 [cond-mat] (2024). <https://doi.org/10.48550/arXiv.2404.05644> . <http://arxiv.org/abs/2404.05644> Accessed 2024-05-17
- [111] Blazquez, S., Conde, M.M., Abascal, J.L.F., Vega, C.: The Madrid-2019 force field for electrolytes in water using TIP4P/2005 and scaled charges: Extension to the ions F⁻, Br⁻, I⁻, Rb⁺, and Cs⁺. *The Journal of Chemical Physics* **156**(4), 044505 (2022) <https://doi.org/10.1063/5.0077716> . Accessed 2023-07-17
- [112] Zeron, I.M., Abascal, J.L.F., Vega, C.: A force field of Li⁺, Na⁺, K⁺, Mg²⁺, Ca²⁺, Cl⁻, and SO₄²⁻ in aqueous solution based on the TIP4P/2005 water model and scaled charges for the ions. *The Journal of Chemical Physics* **151**(13),

134504 (2019) <https://doi.org/10.1063/1.5121392> . Accessed 2023-07-17

- [113] Kanak, A., Kopach, O., Kanak, L., Levchuk, I., Isaiev, M., Brabec, C.J., Fochuk, P., Khalavka, Y.: Melting and Crystallization Features of CsPbBr₃ Perovskite. *Crystal Growth & Design* **22**(7), 4115–4121 (2022) <https://doi.org/10.1021/acs.cgd.1c01530> . Accessed 2022-10-13
- [114] Zhang, M., Zheng, Z., Fu, Q., Chen, Z., He, J., Zhang, S., Chen, C., Luo, W.: Synthesis and single crystal growth of perovskite semiconductor CsPbBr₃. *Journal of Crystal Growth* **484**, 37–42 (2018) <https://doi.org/10.1016/j.jcrysgro.2017.12.020> . Accessed 2023-07-18
- [115] Batzner, S., Musaelian, A., Sun, L., Geiger, M., Mailoa, J.P., Kornbluth, M., Molinari, N., Smidt, T.E., Kozinsky, B.: E(3)-equivariant graph neural networks for data-efficient and accurate interatomic potentials. *Nature Communications* **13**(1), 2453 (2022) <https://doi.org/10.1038/s41467-022-29939-5> . Accessed 2024-04-23
- [116] Humphrey, W., Dalke, A., Schulten, K.: VMD: Visual molecular dynamics. *Journal of Molecular Graphics* **14**(1), 33–38 (1996) [https://doi.org/10.1016/0263-7855\(96\)00018-5](https://doi.org/10.1016/0263-7855(96)00018-5) . Accessed 2023-02-27
- [117] Bartók, A.P., Kondor, R., Csányi, G.: On representing chemical environments. *Physical Review B* **87**(18), 184115 (2013) <https://doi.org/10.1103/PhysRevB.87.184115> arXiv:1209.3140v2
- [118] Musil, F., De, S., Yang, J., Campbell, J.E., Day, G.M., Ceriotti, M.: Machine learning for the structure–energy–property landscapes of molecular crystals. *Chemical Science* **9**(5), 1289–1300 (2018) <https://doi.org/10.1039/C7SC04665K>
- [119] Gallet, G.A., Pietrucci, F.: Structural cluster analysis of chemical reactions in solution. *The Journal of Chemical Physics* **139**(7), 074101 (2013) <https://doi.org/10.1063/1.4818005> . Accessed 2024-05-16
- [120] Martelli, F., Ko, H.-Y., Oguz, E.C., Car, R.: Local-order metric for condensed-phase environments. *Phys. Rev. B* **97**, 064105 (2018) <https://doi.org/10.1103/PhysRevB.97.064105>
- [121] Musil, F., Grisafi, A., Bartók, A.P., Ortner, C., Csányi, G., Ceriotti, M.: Physics-Inspired Structural Representations for Molecules and Materials. *Chemical Reviews* **121**(16), 9759–9815 (2021) <https://doi.org/10.1021/acs.chemrev.1c00021> arXiv:2101.04673
- [122] Tribello, G.A., Bonomi, M., Branduardi, D., Camilloni, C., Bussi, G.: PLUMED 2: New feathers for an old bird. *Computer Physics Communications* **185**(2), 604–613 (2014) <https://doi.org/10.1016/j.cpc.2013.09.018> . Accessed 2024-05-17

- [123] Bonomi, M., Branduardi, D., Bussi, G., Camilloni, C., Provasi, D., Raiteri, P., Donadio, D., Marinelli, F., Pietrucci, F., Broglia, R.A., Parrinello, M.: PLUMED: A portable plugin for free-energy calculations with molecular dynamics. *Computer Physics Communications* **180**(10), 1961–1972 (2009) <https://doi.org/10.1016/j.cpc.2009.05.011> . Accessed 2024-05-17
- [124] Thind, A.S., Luo, G., Hachtel, J.A., Morrell, M.V., Cho, S.B., Borisevich, A.Y., Idrobo, J., Xing, Y., Mishra, R.: Atomic Structure and Electrical Activity of Grain Boundaries and Ruddlesden–Popper Faults in Cesium Lead Bromide Perovskite. *Advanced Materials* **31**(4), 1805047 (2019) <https://doi.org/10.1002/adma.201805047> . Accessed 2023-07-26
- [125] Wang, L., Li, L., Jia, S., Meng, W., Cheng, Y., Liu, Z., Li, L., Yan, S., Gao, Y., Wang, J., Tang, J.: Tailoring of Photoluminescence Properties in All-Vacuum Deposited Perovskite via Ruddlesden–Popper Faults. *Advanced Functional Materials* **33**(6), 2210286 (2023) <https://doi.org/10.1002/adfm.202210286> . Accessed 2023-07-26
- [126] Kim, H.-S., An, J.-S., Bae, H.B., Chung, S.-Y.: Atomic-scale observation of premelting at 2D lattice defects inside oxide crystals. *Nature Communications* **14**(1), 2255 (2023) <https://doi.org/10.1038/s41467-023-37977-w> . Accessed 2024-03-01
- [127] Shi, L.: Premelting occurs at 2D faults. *Nature Nanotechnology* **18**(6), 552–552 (2023) <https://doi.org/10.1038/s41565-023-01426-y> . Accessed 2024-03-01
- [128] Lee, K., Wang, B.Y., Osada, M., Goodge, B.H., Wang, T.C., Lee, Y., Harvey, S., Kim, W.J., Yu, Y., Murthy, C., Raghu, S., Kourkoutis, L.F., Hwang, H.Y.: Linear-in-temperature resistivity for optimally superconducting (Nd,Sr)NiO₂. *Nature* **619**(7969), 288–292 (2023) <https://doi.org/10.1038/s41586-023-06129-x> . Accessed 2024-03-01
- [129] Chen, S., Dai, X., Xu, S., Jiao, H., Zhao, L., Huang, J.: Stabilizing perovskite-substrate interfaces for high-performance perovskite modules. *Science* **373**(6557), 902–907 (2021) <https://doi.org/10.1126/science.abi6323> . Accessed 2024-02-29
- [130] Dzhigaev, D., Zhang, Z., Marçal, L.A.B., Sala, S., Björling, A., Mikkelsen, A., Wallentin, J.: Three-dimensional coherent x-ray diffraction imaging of ferroelastic domains in single CsPbBr₃ perovskite nanoparticles. *New Journal of Physics* **23**(6), 063035 (2021) <https://doi.org/10.1088/1367-2630/ac02e0> . Accessed 2024-03-01
- [131] Song, K., Liu, J., Lu, N., Qi, D., Qin, W.: Direct atomic-scale imaging of a screw dislocation core structure in inorganic halide perovskites. *Physical Chemistry Chemical Physics* **24**(11), 6393–6397 (2022) <https://doi.org/10.1039/D2CP00183G> . Accessed 2024-03-01

- [132] Orr, K.W.P., Diao, J., Lintangpradipto, M.N., Batey, D.J., Iqbal, A.N., Kahmann, S., Frohma, K., Dubajic, M., Zelewski, S.J., Dearle, A.E., Selby, T.A., Li, P., Doherty, T.A.S., Hofmann, S., Bakr, O.M., Robinson, I.K., Stranks, S.D.: Imaging Light-Induced Migration of Dislocations in Halide Perovskites with 3D Nanoscale Strain Mapping (2023) <https://doi.org/10.48550/ARXIV.2304.09554> . Accessed 2023-07-30
- [133] Macpherson, S., Doherty, T.A.S., Winchester, A.J., Kosar, S., Johnstone, D.N., Chiang, Y.-H., Galkowski, K., Anaya, M., Frohma, K., Iqbal, A.N., Nagane, S., Roose, B., Andaji-Garmaroudi, Z., Orr, K.W.P., Parker, J.E., Midgley, P.A., Dani, K.M., Stranks, S.D.: Local nanoscale phase impurities are degradation sites in halide perovskites. *Nature* **607**(7918), 294–300 (2022) <https://doi.org/10.1038/s41586-022-04872-1> . Accessed 2024-03-01
- [134] Kroemer, H.: Polar-on-nonpolar epitaxy. *Journal of Crystal Growth* **81**(1-4), 193–204 (1987) [https://doi.org/10.1016/0022-0248\(87\)90391-5](https://doi.org/10.1016/0022-0248(87)90391-5) . Accessed 2024-05-17
- [135] Alferov, Z.I.: The history and future of semiconductor heterostructures from the point of view of a Russian scientist. *Physica Scripta* **T68**, 32–45 (1996) <https://doi.org/10.1088/0031-8949/1996/T68/005> . Accessed 2024-05-17
- [136] Shuji Nakamura, S.N.: GaN Growth Using GaN Buffer Layer. *Japanese Journal of Applied Physics* **30**(10A), 1705 (1991) <https://doi.org/10.1143/JJAP.30.L1705> . Accessed 2023-07-12
- [137] Amano, H., Sawaki, N., Akasaki, I., Toyoda, Y.: Metalorganic vapor phase epitaxial growth of a high quality GaN film using an AlN buffer layer. *Applied Physics Letters* **48**(5), 353–355 (1986) <https://doi.org/10.1063/1.96549> . Accessed 2023-06-19
- [138] Oliver, R.A., Kappers, M.J., Humphreys, C.J., Briggs, G.A.D.: Growth modes in heteroepitaxy of InGaN on GaN. *Journal of Applied Physics* **97**(1), 013707 (2005) <https://doi.org/10.1063/1.1823581> . Accessed 2024-05-17
- [139] Song, J., Li, Q., Wang, X., Li, J., Zhang, S., Kjems, J., Besenbacher, F., Dong, M.: Evidence of Stranski–Krastanov growth at the initial stage of atmospheric water condensation. *Nature Communications* **5**(1), 4837 (2014) <https://doi.org/10.1038/ncomms5837> . Accessed 2024-04-23
- [140] Zhang, S., Ye, F., Wang, X., Chen, R., Zhang, H., Zhan, L., Jiang, X., Li, Y., Ji, X., Liu, S., Yu, M., Yu, F., Zhang, Y., Wu, R., Liu, Z., Ning, Z., Neher, D., Han, L., Lin, Y., Tian, H., Chen, W., Stolterfoht, M., Zhang, L., Zhu, W.-H., Wu, Y.: Minimizing buried interfacial defects for efficient inverted perovskite solar cells. *Science* **380**(6643), 404–409 (2023) <https://doi.org/10.1126/science.adg3755> . Accessed 2024-02-28

- [141] Azmi, R., Utomo, D.S., Vishal, B., Zhumagali, S., Dally, P., Risqi, A.M., Praseutto, A., Ugur, E., Cao, F., Imran, I.F., Said, A.A., Pininti, A.R., Subbiah, A.S., Aydin, E., Xiao, C., Il Seok, S., De Wolf, S.: Double-side 2-dimensional/3-dimensional heterojunctions for inverted perovskite solar cells. *Nature* (2024) <https://doi.org/10.1038/s41586-024-07189-3> . Accessed 2024-02-28
- [142] Gao, H., Xiao, K., Lin, R., Zhao, S., Wang, W., Dayneko, S., Duan, C., Ji, C., Sun, H., Bui, A.D., Liu, C., Wen, J., Kong, W., Luo, H., Zheng, X., Liu, Z., Nguyen, H., Xie, J., Li, L., Saidaminov, M.I., Tan, H.: Homogeneous crystallization and buried interface passivation for perovskite tandem solar modules. *Science* **383**(6685), 855–859 (2024) <https://doi.org/10.1126/science.adj6088> . Accessed 2024-02-28
- [143] Xu, W., Chen, B., Zhang, Z., Liu, Y., Xian, Y., Wang, X., Shi, Z., Gu, H., Fei, C., Li, N., Uddin, M.A., Zhang, H., Dou, L., Yan, Y., Huang, J.: Multifunctional entinostat enhances the mechanical robustness and efficiency of flexible perovskite solar cells and minimodules. *Nature Photonics* (2024) <https://doi.org/10.1038/s41566-023-01373-z> . Accessed 2024-02-29
- [144] Filip, M.-A., Scott, C.J.C., Thom, A.J.W.: Multireference stochastic coupled cluster. *Journal of Chemical Theory and Computation* **15**(12), 6625–6635 (2019) <https://doi.org/10.1021/acs.jctc.9b00741> <https://doi.org/10.1021/acs.jctc.9b00741>
- [145] Nagy, P.R., Kállay, M.: Approaching the Basis Set Limit of CCSD(T) Energies for Large Molecules with Local Natural Orbital Coupled-Cluster Methods. *Journal of Chemical Theory and Computation* **15**(10), 5275–5298 (2019) <https://doi.org/10.1021/acs.jctc.9b00511> . Accessed 2024-03-01
- [146] Zhang, I.Y., Grüneis, A.: Coupled Cluster Theory in Materials Science. *Frontiers in Materials* **6**, 123 (2019) <https://doi.org/10.3389/fmats.2019.00123> . Accessed 2024-03-01
- [147] Booth, G.H., Grüneis, A., Kresse, G., Alavi, A.: Towards an exact description of electronic wavefunctions in real solids. *Nature* **493**(7432), 365–370 (2013) <https://doi.org/10.1038/nature11770> . Accessed 2024-03-01
- [148] Katukuri, V.M., Bogdanov, N.A., Alavi, A.: Ab Initio Wavefunction Analysis of Electron Removal Quasi-Particle State of NdNiO₂ With Fully Correlated Quantum Chemical Methods. *Frontiers in Physics* **10**, 836784 (2022) <https://doi.org/10.3389/fphy.2022.836784> . Accessed 2024-03-01
- [149] Cui, Z.-H., Zhai, H., Zhang, X., Chan, G.K.-L.: Systematic electronic structure in the cuprate parent state from quantum many-body simulations. *Science* **377**(6611), 1192–1198 (2022) <https://doi.org/10.1126/science.abm2295> . Accessed 2024-03-01

- [150] Filip, M.-A., Thom, A.J.W.: A hybrid stochastic configuration interaction–coupled cluster approach for multireference systems. *The Journal of Chemical Physics* **158**(18), 184101 (2023) <https://doi.org/10.1063/5.0145767> . Accessed 2024-02-29
- [151] Zhao, Z., Filip, M.-A., Thom, A.J.W.: Rapidly convergent coupled-cluster Monte Carlo using a Chebyshev projector (2024) <https://doi.org/10.48550/ARXIV.2402.16685> . Accessed 2024-02-29
- [152] Fan, Z., Chen, W., Vierimaa, V., Harju, A.: Efficient molecular dynamics simulations with many-body potentials on graphics processing units. *Computer Physics Communications* **218**, 10–16 (2017) <https://doi.org/10.1016/j.cpc.2017.05.003> . Accessed 2024-02-29
- [153] Thölke, P., De Fabritiis, G.: TorchMD-NET: Equivariant Transformers for Neural Network based Molecular Potentials. arXiv. arXiv:2202.02541 [physics] version: 2 (2022). <https://doi.org/10.48550/arXiv.2202.02541> . <http://arxiv.org/abs/2202.02541> Accessed 2024-04-26
- [154] Musaelian, A., Batzner, S., Johansson, A., Sun, L., Owen, C.J., Kornbluth, M., Kozinsky, B.: Learning local equivariant representations for large-scale atomistic dynamics. *Nature Communications* **14**(1), 579 (2023) <https://doi.org/10.1038/s41467-023-36329-y> . Accessed 2024-02-29
- [155] Gong, S., Zhang, Y., Mu, Z., Pu, Z., Wang, H., Yu, Z., Chen, M., Zheng, T., Wang, Z., Chen, L., Wu, X., Shi, S., Gao, W., Yan, W., Xiang, L.: BAMBOO: a predictive and transferable machine learning force field framework for liquid electrolyte development. arXiv. arXiv:2404.07181 [cond-mat, physics:physics] version: 4 (2024). <https://doi.org/10.48550/arXiv.2404.07181> . <http://arxiv.org/abs/2404.07181> Accessed 2024-04-26
- [156] Bednorz, J.G., Müller, K.A.: Perovskite-type oxides—The new approach to high-T_c superconductivity. *Reviews of Modern Physics* **60**(3), 585–600 (1988) <https://doi.org/10.1103/RevModPhys.60.585> . Accessed 2023-06-16
- [157] Cava, R.J., Batlogg, B., Krajewski, J.J., Farrow, R., Rupp, L.W., White, A.E., Short, K., Peck, W.F., Kometani, T.: Superconductivity near 30 K without copper: the Ba_{0.6}K_{0.4}BiO₃ perovskite. *Nature* **332**(6167), 814–816 (1988) <https://doi.org/10.1038/332814a0> . Accessed 2023-06-16
- [158] Li, L., Richter, C., Mannhart, J., Ashoori, R.C.: Coexistence of magnetic order and two-dimensional superconductivity at LaAlO₃/SrTiO₃ interfaces. *Nature Physics* **7**(10), 762–766 (2011) <https://doi.org/10.1038/nphys2080> . Accessed 2023-06-16
- [159] He, S., He, J., Zhang, W., Zhao, L., Liu, D., Liu, X., Mou, D., Ou, Y.-B., Wang, Q.-Y., Li, Z., Wang, L., Peng, Y., Liu, Y., Chen, C., Yu, L., Liu, G.,

- Dong, X., Zhang, J., Chen, C., Xu, Z., Chen, X., Ma, X., Xue, Q., Zhou, X.J.: Phase diagram and electronic indication of high-temperature superconductivity at 65 K in single-layer FeSe films. *Nature Materials* **12**(7), 605–610 (2013) <https://doi.org/10.1038/nmat3648> . Accessed 2023-06-19
- [160] Wang, J., Neaton, J.B., Zheng, H., Nagarajan, V., Ogale, S.B., Liu, B., Viehland, D., Vaithyanathan, V., Schlom, D.G., Waghmare, U.V., Spaldin, N.A., Rabe, K.M., Wuttig, M., Ramesh, R.: Epitaxial BiFeO₃ Multiferroic Thin Film Heterostructures. *Science* **299**(5613), 1719–1722 (2003) <https://doi.org/10.1126/science.1080615> . Accessed 2023-06-16
- [161] Hilgenkamp, H., Mannhart, J.: Grain boundaries in high- T_c superconductors. *Reviews of Modern Physics* **74**(2), 485–549 (2002) <https://doi.org/10.1103/RevModPhys.74.485> . Accessed 2023-06-16
- [162] Li, Y., Zhou, W., Xin, S., Li, S., Zhu, J., Lü, X., Cui, Z., Jia, Q., Zhou, J., Zhao, Y., Goodenough, J.B.: Fluorine-Doped Antiperovskite Electrolyte for All-Solid-State Lithium-Ion Batteries. *Angewandte Chemie International Edition* **55**(34), 9965–9968 (2016) <https://doi.org/10.1002/anie.201604554> . Accessed 2023-06-16
- [163] Lai, K.T., Antonyshyn, I., Prots, Y., Valldor, M.: Anti -Perovskite Li-Battery Cathode Materials. *Journal of the American Chemical Society* **139**(28), 9645–9649 (2017) <https://doi.org/10.1021/jacs.7b04444> . Accessed 2023-06-16
- [164] Li, Y., Xu, H., Chien, P., Wu, N., Xin, S., Xue, L., Park, K., Hu, Y., Goodenough, J.B.: A Perovskite Electrolyte That Is Stable in Moist Air for Lithium-Ion Batteries. *Angewandte Chemie International Edition* **57**(28), 8587–8591 (2018) <https://doi.org/10.1002/anie.201804114> . Accessed 2023-06-16
- [165] Xu, H., Chien, P.-H., Shi, J., Li, Y., Wu, N., Liu, Y., Hu, Y.-Y., Goodenough, J.B.: High-performance all-solid-state batteries enabled by salt bonding to perovskite in poly(ethylene oxide). *Proceedings of the National Academy of Sciences* **116**(38), 18815–18821 (2019) <https://doi.org/10.1073/pnas.1907507116> . Accessed 2023-06-16
- [166] Huang, Y.-H., Dass, R.I., Xing, Z.-L., Goodenough, J.B.: Double Perovskites as Anode Materials for Solid-Oxide Fuel Cells. *Science* **312**(5771), 254–257 (2006) <https://doi.org/10.1126/science.1125877> . Accessed 2023-06-16
- [167] Ashoka, A., Nagane, S., Strkalj, N., Sharma, A., Roose, B., Sneyd, A.J., Sung, J., MacManus-Driscoll, J.L., Stranks, S.D., Feldmann, S., Rao, A.: Local symmetry breaking drives picosecond spin domain formation in polycrystalline halide perovskite films. *Nature Materials* (2023) <https://doi.org/10.1038/s41563-023-01550-z> . Accessed 2023-06-16
- [168] Roos, B.O., Taylor, P.R., Sigbahn, P.E.M.: A complete active space scf method

- (casscf) using a density matrix formulated super-ci approach. *Chem. Phys.* **48**(2), 157–173 (1980) [https://doi.org/10.1016/0301-0104\(80\)80045-0](https://doi.org/10.1016/0301-0104(80)80045-0)
- [169] Siegbahn, P., Heiberg, A., Roos, B., Levy, B.: A comparison of the super-ci and the newton-raphson scheme in the complete active space scf method. *Physica Scripta* **21**(3-4), 323 (1980) <https://doi.org/10.1088/0031-8949/21/3-4/014>
- [170] Siegbahn, P.E.M., Almlöf, J., Heiberg, A., Roos, B.O.: The complete active space SCF (CASSCF) method in a Newton–Raphson formulation with application to the HNO molecule. *The Journal of Chemical Physics* **74**(4), 2384–2396 (1981) <https://doi.org/10.1063/1.441359> https://pubs.aip.org/aip/jcp/article-pdf/74/4/2384/18926917/2384_1_online.pdf
- [171] Hartree, D.R.: The wave mechanics of an atom with a non-coulomb central field. part i. theory and methods. *Mathematical Proceedings of the Cambridge Philosophical Society* **24**(1), 89–110 (1928) <https://doi.org/10.1017/S0305004100011919>
- [172] Fock, V.: Näherungsmethode zur lösung des quantenmechanischen mehrkörperproblems. *Z. Physik* **61**, 126–148 (1930) <https://doi.org/10.1007/BF01340294>
- [173] Roothaan, C.C.J.: New developments in molecular orbital theory. *Rev. Mod. Phys.* **23**, 69–89 (1951) <https://doi.org/10.1103/RevModPhys.23.69>
- [174] Roothaan, C.C.J.: Self-consistent field theory for open shells of electronic systems. *Rev. Mod. Phys.* **32**, 179–185 (1960) <https://doi.org/10.1103/RevModPhys.32.179>
- [175] Leininger, T., Nicklass, A., Küchle, W., Stoll, H., Dolg, M., Bergner, A.: The accuracy of the pseudopotential approximation: non-frozen-core effects for spectroscopic constants of alkali fluorides xf (x = k, rb, cs). *Chem. Phys. Lett.* **255**, 274–280 (1996) [https://doi.org/10.1016/0009-2614\(96\)00382-x](https://doi.org/10.1016/0009-2614(96)00382-x)
- [176] Weigend, F., Ahlrichs, R.: Balanced basis sets of split valence, triple zeta valence and quadruple zeta valence quality for h to rn: Design and assessment of accuracy. *Phys. Chem. Chem. Phys.* **7**, 3297 (2005) <https://doi.org/10.1039/b508541a>
- [177] Metz, B., Stoll, H., Dolg, M.: Small-core multiconfiguration-dirac-hartree-fock-adjusted pseudopotentials for post-d main group elements: Application to pbh and pbo. *J. Chem. Phys.* **113**, 2563–2569 (2000) <https://doi.org/10.1063/1.1305880>
- [178] Sun, Q., Zhang, X., Banerjee, S., Bao, P., Barbry, M., Blunt, N.S., Bogdanov, N.A., Booth, G.H., Chen, J., Cui, Z.-H., Eriksen, J.J., Gao, Y., Guo, S., Hermann, J., Hermes, M.R., Koh, K., Koval, P., Lehtola, S., Li, Z., Liu, J., Mardirossian, N., McClain, J.D., Motta, M., Mussard, B.,

- Pham, H.Q., Pulkin, A., Purwanto, W., Robinson, P.J., Ronca, E., Sayfutyarova, E.R., Scheurer, M., Schurkus, H.F., Smith, J.E.T., Sun, C., Sun, S.-N., Upadhyay, S., Wagner, L.K., Wang, X., White, A., Whitfield, J.D., Williamson, M.J., Wouters, S., Yang, J., Yu, J.M., Zhu, T., Berkelbach, T.C., Sharma, S., Sokolov, A.Y., Chan, G.K.-L.: Recent developments in the PySCF program package. *The Journal of Chemical Physics* **153**(2), 024109 (2020) <https://doi.org/10.1063/5.0006074> https://pubs.aip.org/aip/jcp/article-pdf/doi/10.1063/5.0006074/16722275/024109_1_online.pdf
- [179] Dobrautz, W., Weser, O., Bogdanov, N.A., Alavi, A., Li Manni, G.: Spin-pure stochastic-casscf via guga-fciqmc applied to iron–sulfur clusters. *Journal of Chemical Theory and Computation* **17**(9), 5684–5703 (2021) <https://doi.org/10.1021/acs.jctc.1c00589> <https://doi.org/10.1021/acs.jctc.1c00589>
- [180] Weser, O., Guthier, K., Ghanem, K., Li Manni, G.: Stochastic generalized active space self-consistent field: Theory and application. *Journal of Chemical Theory and Computation* **18**(1), 251–272 (2022) <https://doi.org/10.1021/acs.jctc.1c00936> <https://doi.org/10.1021/acs.jctc.1c00936>
- [181] Geiger, M., Smidt, T., M., A., Miller, B.K., Boomsma, W., Dice, B., Lapcheyvskyi, K., Weiler, M., Tyszkiewicz, M., Batzner, S., Madisetti, D., Uhrin, M., Frellsen, J., Jung, N., Sanborn, S., Wen, M., Rackers, J., Rød, M., Bailey, M.: Euclidean Neural Networks: E3nn. <https://doi.org/10.5281/zenodo.6459381> . <https://doi.org/10.5281/zenodo.6459381>
- [182] Geiger, M., Smidt, T.: e3nn: Euclidean Neural Networks. arXiv (2022). <https://doi.org/10.48550/ARXIV.2207.09453> . <https://arxiv.org/abs/2207.09453>
- [183] Ning, J., Kothakonda, M., Furness, J.W., Kaplan, A.D., Ehlert, S., Brandenburg, J.G., Perdew, J.P., Sun, J.: Workhorse minimally empirical dispersion-corrected density functional with tests for weakly bound systems: r² SCAN + rVV 10. *Physical Review B* **106**(7), 075422 (2022) <https://doi.org/10.1103/PhysRevB.106.075422> . Accessed 2024-04-23
- [184] Kresse, G., Hafner, J.: *Ab initio* molecular dynamics for liquid metals. *Physical Review B* **47**(1), 558–561 (1993) <https://doi.org/10.1103/PhysRevB.47.558> . Accessed 2024-04-23
- [185] Kresse, G., Furthmüller, J.: Efficiency of ab-initio total energy calculations for metals and semiconductors using a plane-wave basis set. *Computational Materials Science* **6**(1), 15–50 (1996) [https://doi.org/10.1016/0927-0256\(96\)00008-0](https://doi.org/10.1016/0927-0256(96)00008-0) . Accessed 2024-04-23
- [186] Parrinello, M., Rahman, A.: Polymorphic transitions in single crystals: A new molecular dynamics method. *Journal of Applied Physics* **52**(12), 7182–7190 (1981) <https://doi.org/10.1063/1.328693> . Accessed 2024-04-23

- [187] Steinhardt, P.J., Nelson, D.R., Ronchetti, M.: Bond-orientational order in liquids and glasses. *Physical Review B* **28**(2), 784–805 (1983) <https://doi.org/10.1103/PhysRevB.28.784> . Accessed 2022-10-17
- [188] Lechner, W., Dellago, C.: Accurate determination of crystal structures based on averaged local bond order parameters. *The Journal of Chemical Physics* **129**(11), 114707 (2008) <https://doi.org/10.1063/1.2977970> . Accessed 2022-10-17
- [189] Yu, T.-Q., Chen, P.-Y., Chen, M., Samanta, A., Vanden-Eijnden, E., Tuckerman, M.: Order-parameter-aided temperature-accelerated sampling for the exploration of crystal polymorphism and solid-liquid phase transitions. *The Journal of Chemical Physics* **140**(21), 214109 (2014) <https://doi.org/10.1063/1.4878665> . Accessed 2022-10-17
- [190] Chen, Y., Yao, Z., Tang, S., Tong, H., Yanagishima, T., Tanaka, H., Tan, P.: Morphology selection kinetics of crystallization in a sphere. *Nature Physics* **17**(1), 121–127 (2021) <https://doi.org/10.1038/s41567-020-0991-9> . Accessed 2022-10-17
- [191] Rogal, J.: Reaction coordinates in complex systems-a perspective. *The European Physical Journal B* **94**(11), 223 (2021) <https://doi.org/10.1140/epjb/s10051-021-00233-5> . Accessed 2022-10-17
- [192] Musil, F., Veit, M., Goscinski, A., Fraux, G., Willatt, M.J., Stricker, M., Junge, T., Ceriotti, M.: Efficient implementation of atom-density representations. *Journal of Chemical Physics* **154**(11), 114109 (2021) <https://doi.org/10.1063/5.0044689> arXiv:2101.08814
- [193] De, S., Musil, F., Ingram, T., Baldauf, C., Ceriotti, M.: Mapping and classifying molecules from a high-throughput structural database. *Journal of Cheminformatics* **9**(1), 6 (2017) <https://doi.org/10.1186/s13321-017-0192-4> arXiv:1611.06246
- [194] Bussi, G., Donadio, D., Parrinello, M.: Canonical sampling through velocity rescaling. *The Journal of Chemical Physics* **126**(1), 014101 (2007) <https://doi.org/10.1063/1.2408420> . Accessed 2024-04-23
- [195] Thompson, A.P., Aktulga, H.M., Berger, R., Bolintineanu, D.S., Brown, W.M., Crozier, P.S., In 'T Veld, P.J., Kohlmeyer, A., Moore, S.G., Nguyen, T.D., Shan, R., Stevens, M.J., Tranchida, J., Trott, C., Plimpton, S.J.: LAMMPS - a flexible simulation tool for particle-based materials modeling at the atomic, meso, and continuum scales. *Computer Physics Communications* **271**, 108171 (2022) <https://doi.org/10.1016/j.cpc.2021.108171> . Accessed 2024-04-23
- [196] Bandura, A.V., Kubicki, J.D.: Derivation of Force Field Parameters for TiO₂-H₂O Systems from ab Initio Calculations. *The Journal of Physical Chemistry B* **107**(40), 11072–11081 (2003) <https://doi.org/10.1021/jp034093t> . Accessed

2024-05-18

- [197] Matsui, M., Akaogi, M.: Molecular Dynamics Simulation of the Structural and Physical Properties of the Four Polymorphs of TiO₂. *Molecular Simulation* **6**(4-6), 239–244 (1991) <https://doi.org/10.1080/08927029108022432> . Accessed 2024-05-18